ISAS RESEARCH NOTE

ISAS RN 683

Fabrication of the Astro-E Hard X-ray Detector

K. Nakazawa, T. Kamae, K. Makishima, T. Takahashi, T. Murakami, M. Tashiro, Y. Fukazawa, T. Tamura, N. Iyomoto, K. Ebisawa, Y. Ezoe, M. Hamaya, M. Horii, N. Isobe, M.Kokubun, J. Kotoku, A. Kubota, Y. Matsumoto, T. Mizuno, Y. Mizuno, K. Mori, T. Onishi, N. Ota, S. Shinoda, M. Sugiho, K. Taguchi, I. Takahashi, M. Tanaka, C. Tanihata, Y. Terada, Y. Uchiyama, S. Watanabe, K. Yamaoka, D. Yonetoku

Preflight Performance of the Astro-E Hard X-ray Detector

C. Tanihata, J. Kataoka, T. Murakami, N. Ota, H. Ozawa, T. Takahashi, T. Tamura, Y. Uchiyama, S. Watanabe, K. Yamaoka, D. Yonetoku, Y. Ezoe, Y. Fukazawa, N. Isobe, N. Iyomoto, T. Kamae, M. Kokubun, J. Kotoku, A. Kubota, K. Makishima, Y. Matsumoto, T. Mizuno, K. Nakazawa, T. Onishi, M. Sugiho, I. Takahashi, M. Tanaka, M. Tashiro, Y. Terada, M. Nomachi, A. Yoshida, M. Hamaya, M. Horii, K. Taguchi, N. Morita, I. Odagi, K. Sato, Y. Tanaka, and K. Mori

THE INSTITUTE OF SPACE AND ASTRONAUTICAL SCIENCE

THE INSTITUTE OF SPACE AND ASTRONAUTICAL SCIENCE
YOSHINODAI, SAGAMIHARA, KANAGAWA 229-8510

ISAS RESEARCH NOTE

ISAS RN 685

Fabrication of the Astro-E Hard X-ray Detector

K. Nakazawa, T. Kamae, K. Makishima, T. Takahashi, T. Murakami, M. Tashiro, Y. Fukazawa, T. Tamura, N. Iyomoto, K. Ebisawa, Y. Ezoe,M. Hamaya, M. Horii, N. Isobe,M. Kokubun, J. Kotoku, A. Kubota, Y. Matumoto, T. Mizuno, Y. Mizuno, K. Mori T. Onishi, N. Ota, S. Shinoda, M. Sugiho, K. Taguchi, I. Takahasi, M. Tanaka, C. Tanihata, Y. Terada, Y. Uchiyama, S. Watanabe, K. Yamaoka, D. Yonetoku

Preflight Performance of the Astro-E Hard X-ray Detector

C. Tanihata, J. Kataoka, T. Murakami, N. Ota, H. Ozawa, T. Takahashi, T. Tamura, Y. Uchiyama, S. Watanabe, K. Yamaoka, D. Yonetoku, Y. Ezoe, Y. Fukazawa, N. Isobe, N. Iyomoto, T. Kamae, M. Kokubun, J. Kotoku, A. Kubota, K. Makishima, Y. Matsumoto, T. Mizuno, K. Nakazawa, T. Onishi, M. Sugiho, I. Takahashi, M. Tanaka, M. Tashiro, Y. Terada, M. Nomachi, A. Yoshida, M. Hamaya, M. Horii, K. Taguchi, N. Morita, I. Odagi, K. Sato, Y. Tanaka, and K. Mori

August 1999

to appear in SPIE 3765, 1999

Fabrication of the ASTRO-E Hard X-ray Detector

K. Nakazawa[a], T. Kamae[a], K. Makishima[a], T. Takahashi[b], T. Murakami[b],
M. Tashiro[a], Y. Fukazawa[a], T. Tamura[b], N. Iyomoto[a],
K. Ebisawa[c], Y. Ezoe[a],M. Hamaya[c], M. Horii[c], N. Isobe[a],M. Kokubun[a],
J. Kotoku[a], A. Kubota[a], Y. Matumoto[a], T. Mizuno[a], Y. Mizuno[b], K. Mori[d],
T. Onishi[a], N. Ota[b], S. Shinoda[c],M. Sugiho[a], K. Taguchi[c], I. Takahasi[a],
M. Tanaka[a], C. Tanihata[b], Y. Terada[a], Y. Uchiyama[b], S. Watanabe[b], K. Yamaoka[b], D. Yonetoku[b]

[a]Department of Physics, University of Tokyo
7-3-1 Hongo, Bunkyo-ku, Tokyo, Japan 113

[b]Institute of Space and Astronautical Science (ISAS)
3-1-1 Yoshinodai, Sagamihara,kanagawa, JAPAN 229

[c]Meisei Electric Company Ltd.
249-1 Moriya-Kou, Moriya, Kitasouma-gun,Ibaraki, 302-0115, Japan

[d]Clear Pulse Company Ltd.
6-25-17, Chuo, Ohta-ku, Tokyo, 143-0024, Japan

ABSTRACT

The Hard X-ray Detector (HXD) is one of the three instruments on the fifth Japanese cosmic X-ray satellite ASTRO-E, scheduled for launch in January, 2000. The HXD covers a wide energy range of 10−600 keV, using 16 identical GSO/BGO phoswich-counter modules, of which the low-energy efficiency is greatly improved by adding 2 mm-thick silicon PIN diodes. Production of the HXD has been completed and pre-flight calibration is now in progress. The design concept of the HXD sensor, detail of the production process, and a brief summary of the measured performance is reported.

Keywords: Hard X-ray detector, Gamma-ray Astronomy, BGO/GSO scintillation crystal, Silicon Photo Diode, Astro-E, space environment

1. INTRODUCTION

The fifth Japanese cosmic X-ray satellite, ASTRO-E[1−3] is scheduled for launch in the end of January 2000 by the M-V-4 launcher of Institute of Space and Astronautical Science (ISAS) from Kagoshima Space Center. The satellite is to be thrown into a circular orbit, with an altitude of 550 km and inclination of 31 degrees.

There are three experiments onboard the satellite. A micro-calorimeter array (X-ray Spectrometer – XRS) with an X-ray mirror and 4 CCDs (X-ray Imaging Spectrometer – XIS) with 4 X-ray mirrors cover the soft X-ray band from 0.4 to 12.0 keV. The XRS has the highest energy resolution of $\Delta E \sim 12$eV and the XIS has a good energy resolution of $\Delta E \sim 150$ eV(5.9 keV) with imaging capability. The Hard X-ray detector (HXD) is a collimated counter array which covers the energy band from 10 to 600 keV. Combining these three experiments, ASTRO-E becomes a highly sensitive spectrometer facility, covering a wide energy band from 0.4 to 600 keV.

The overall HXD experiment comprises three components; the Sensor (HXD-S), Analog Electronics (HXD-AE) and Digital Electronics (HXD-DE). This paper mainly deals with HXD-S. The production of the flight model of the HXD has started in 1997, and has been completed at May, 1999. The HXD has been mounted on the spacecraft, and the pre-flight tests of the whole spacecraft will continue till the end of this year. We will present the design concept, the production processes and the final configuration of HXD-S, with a brief summary of achieved performance. Details of the pre-flight performance are reported by Tanihata et al. in this volume.

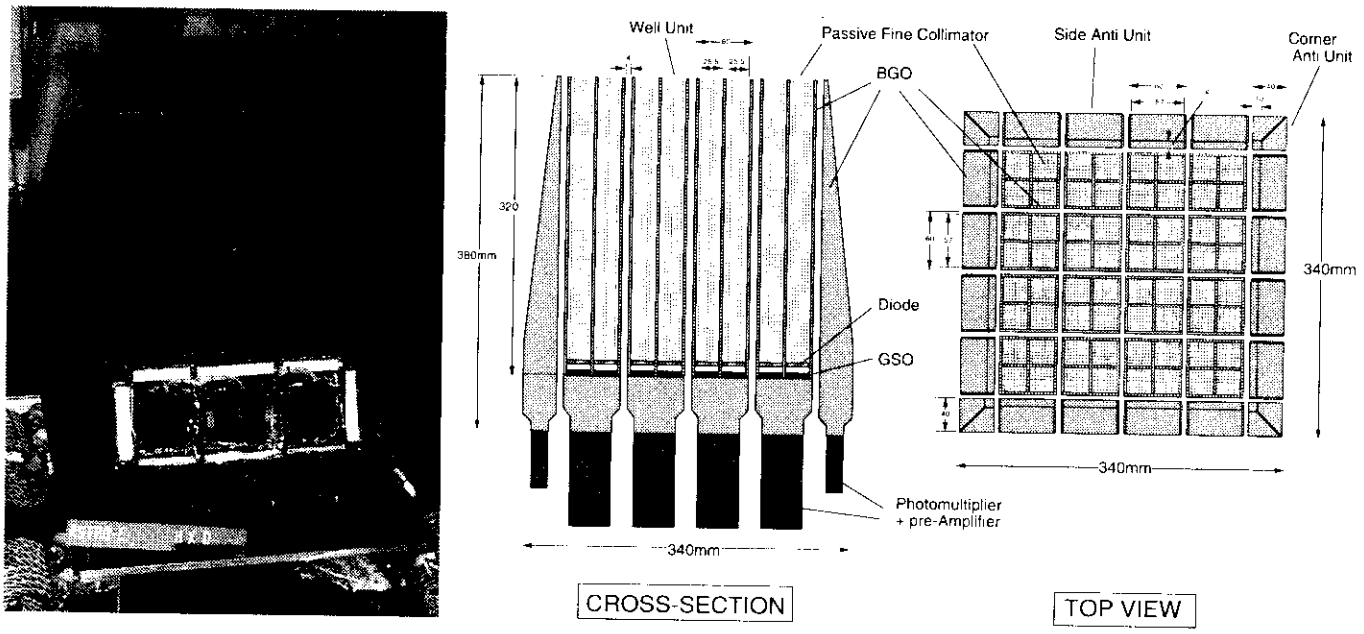

Figure 1. (*left*): The HXD Sensor (HXD-S) placed on its temporary container, ready to be mounted on the satellite. It consists of 36 counters held in the housing. Three of the twelve high-voltage power supply are seen in front. (*right*): A schematic concept of HXD-S. 16 well-type phoswich counters (Well units) are arranged in 4×4 configuration and are surrounded by 20 anti-coincidence counters (Anti units).

2. THE HARD X-RAY DETECTOR

2.1. Overview

The HXD is a cosmic hard X-ray detector instrument employing inorganic scintillators and silicon PIN diodes, and characterized by its extremely low background.[4] The HXD Sensor (HXD-S) consists of 16 well-type phoswich counters (Well units) in 4×4 compound-eye configuration, and 20 anti-coincidence counters (Anti units) surrounding the Well units. A photograph and the schematic illustration of HXD-S are shown in Fig. 1. The whole HXD-S has a dimension of 420 mm × 547 mm × 656 mm, and weighs 186 kg. A summary of the operational parameters of the HXD, based on the the pre-flight calibration are shown in table 1 (see § 7).

Energy Range	10–600 keV (10–60 keV for PIN diodes, 30–600 keV for GSO Scintillators)
Energy Resolution (FWHM)	3.5 keV for the PIN diode $2.4 \times \sqrt{E(\mathrm{keV})}$ keV for the GSO
Effective Area (No alignment correction)	160 cm^2 for the 2 mm thick silicon PIN diode 350 cm^2 for the 5 mm thick GSO
Field of View (FWHM)	$0°.57 \times 0°.57$ ($\leq$ 100 keV), $4°.57 \times 4°.57$ ($\geq$ 100 keV)
Background Rate	$\sim (1-8) \times 10^{-5}$ c sec^{-1} cm^{-2} keV^{-1}
Time Resolution	normally 61μsec (minimum 15.3μsec)

Table 1. Basic parameters of HXD, based on the pre-flight calibration.

The main detection part of each Well unit is made of 5 mm thick GSO (Gd_2SiO_5:Ce 0.5% mol) scintillation crystal,[7–10] and 2 mm thick silicon PIN type photo diodes[12–14] mounted in front of the GSO. The PIN diodes cover

the lower energy range, and the GSO detects photons with higher energy range, making the total energy range of the Well unit from 10 to 600 keV. The active shielding part is made of BGO ($Bi_4Ge_3O_{12}$) scintillation crystal,[11] which forms a well-shaped structure with four wells. The GSO and diodes are buried in the bottom of each well and the GSO/BGO crystal forms so called phoswich configuration. The field of view (FOV) of each Well unit is limited to $4°.57 \times 4°.57$ (FWHM) by BGO active shielding. As the cosmic diffuse X-ray background dominates the lower energy band, a fine collimator made of 50 μm thick phosphor bronze sheet is installed in each well, limiting the FOV to $0°.57 \times 0°.57$ (FWHM) in the energy range lower than $\sim$ 100 keV. Photons fully deposited the energy in the GSO or diodes are selected as valid events, while the BGO contaminated events are rejected by pulse shape discrimination. The 16 Well units are arranged in 4×4 matrix to enlarge the detection area, and is used in mutual anti-coincidence.

The Anti units surrounding the Well units are made of thick BGO crystals, and act as active shields for the Well units. Their are also used to guard the Well units from the high energy charged particles both actively and passively, so that radio activation and the background of the detector is suppressed. In addition, the large planes of the Anti units are also used to monitor the transient sources and gamma-ray bursts.

To suppress the leakage current of the PIN diodes and increase their energy resolution, HXD-S is designed to operate at low temperature, around $-20°$C. The light yield and hence the energy resolution of the scintillation crystals also increases at low temperature.

The compound-eye configuration of HXD-S has an important merit. It makes the hardware production easier; it helps the background rejection via mutual anti-coincidence among neighboring detector (Well and Anti) units; and it allows high-speed parallel processing of signals and thus minimize the dead time by high particle event rates (up to $\sim$ 10 kHz anticipated in total).

Total of 116 signal lines come out from HXD-S: 32 lines (anode and last dynode signals) from the 16 Photo Multiplier Tubes (PMTs) of the Well units, 64 lines from the PIN diodes (4 per Well unit), and 20 lines from the PMTs of the Anti units. The signals from the PMT dynode of the Well units go to the pulse shape discrimination circuit in HXD-AE. The circuit selects the pure GSO events using the difference in the decay-time of the scintillation light between GSO ($\tau \sim$ 100 ns at $-20°$C) and BGO ($\tau \sim$ 700 ns at $-20°$C). For detailed information of the data processing, see Takahasi et al. (1998).

2.2. Major Design Features in the Production of HXD-S

Key points in the production of the HXD-S are summarized as follows:

- Mechanical design to protect HXD-S, particularly the dense and brittle BGO crystals, against the vibration and shocks in the launch.
- Thermal design to operate HXD-S at $-20°$C.
- Design of light reflectors to increase the collection efficiency of scintillation lights.
- Electric noise suppression, especially for the PIN diode.
- Alignment of the Well units and fine collimators.
- Choice of materials with the lowest radio isotope contaminations, and low cross sections for the particle-induced radio activation in orbit.

In the following three sections, we will report the detailed design of the Well unit, the Anti unit and the HXD-S housing.

3. PRODUCTION OF THE WELL UNIT

The crystal part of one Well unit is 397 mm long, and 185 mm long PMT plus electronics part is attached on one side. It has 63 mm $\times$ 63 mm square cross section, and weighs 4.63 kg. The crystal part is made of scintillation crystals, PIN diodes, fine collimators and their support structures. Electronics part consists of a PMT, its bleeder, a μ-metal shield, one PMT pre-amplifier and four low noise PIN pre-amplifiers. Total of 19 Well units have been produced including 3 spare units. Schematic drawing and photograph of the Well unit are shown in Fig. 2.

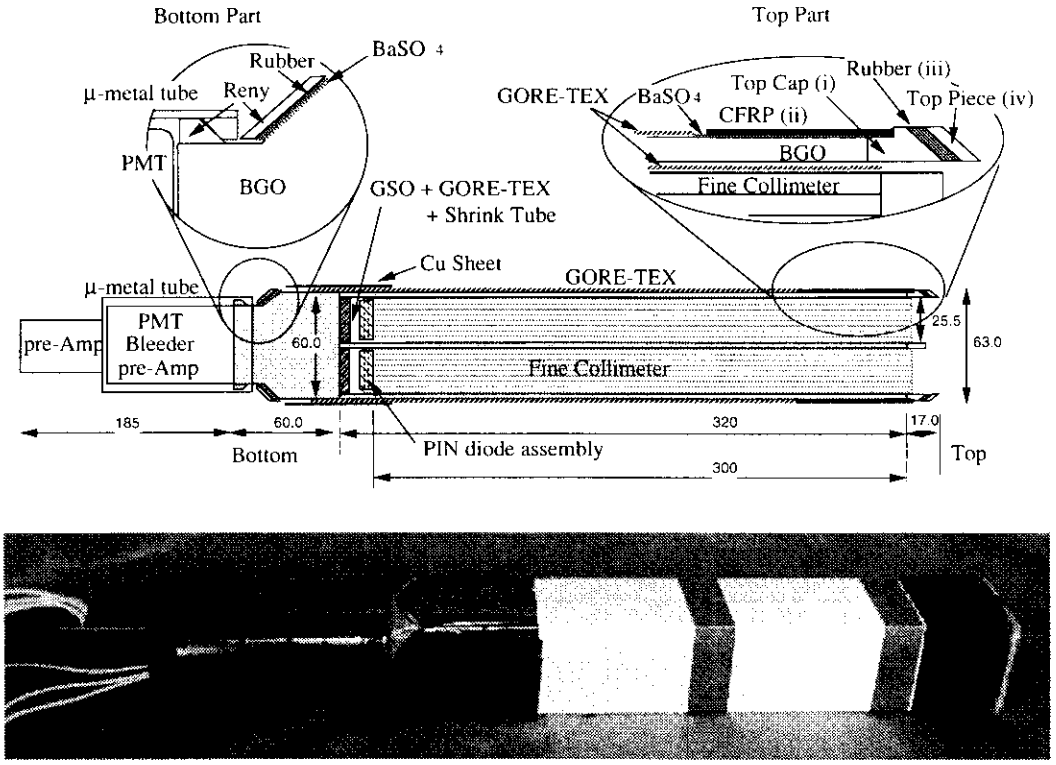

Figure 2. (*top*): Schematic drawing of a Well unit. Crystals, PIN diodes, fine collimators, support structures, reflectors, PMT and front electronics are shown. The active shielding part forms four wells for collimation, on the bottom surface of which the 5 mm thick GSO crystals are glued. The 2 mm thick PIN diode is embedded in the bottom position of each fine collimator. (*bottom*): Photograph of a Well unit.

3.1. Scintillation Crystal

The shielding part of the Well unit is made of seven 3 mm thick BGO plates and a block of BGO. These pieces are glued together by epoxy resin EpoTek 301-2 (Epoxy Technology Inc.) which is transparent in the wavelength of the scintillation light ($\sim$ 400 nm).[15] The active collimation part forms four wells of 320 mm deep and 25.5 mm $\times$ 25.5 mm of cross section. The bottom BGO part, originally a cube of 60 mm in one dimension, is manufactured as a light guide with a conical surface, ending with a cylindrical shape to meet the PMT.

The detection part is made of four GSO crystals, each having a dimension of 24.0 mm $\times$ 24.0 mm $\times$ 5.0 mm. One side of the GSO is glued to the BGO bottom block. We used an elastic silicon compound KE108 (by Shin-Etsu Chemical Co.) to reduce the thermal stress between the two crystals. Remaining five sides of the GSO are covered with GoreTex sheet[?] as a light reflector, which is held by white shrink tube. As the scintillation light from the four GSO is viewed with a single PMT, four crystals with similar light yield at -20°C are grouped, and the thickness of the GoreTex reflector was controlled for precise adjustment of their light yields. The typical light yield of the GSO crystal is around 30 % of a typical NaI (Tl), when directly coupled to the PMT, and we can collect about a half of the light when viewed through the BGO bottom.

3.2. Support Structure of the Well Unit

Each Well unit is separately held at its both ends in the housing structure. This is for easy replacement of any malfunctioning unit. BGO crystal, the main material of the Well unit, is dense (specific weight 7.2) and brittle. In addition, the mechanical vibration test level required for each component is very high, 27 G_{rms} in the 10 - 2000 Hz range. The support structure, therefore, is mainly designed to protect the crystals from the severe mechanical environment. In addition, we have to align the 16 Well units and 64 fine collimators to an accuracy of $\sim 3'$. Taking these requirements into account, we have developed the holding structure shown in Fig. 2 by "top" and "bottom".

The top part of the holding structure consists of (i) a plastic "top cap" segment with a tapered end, (ii) four 1 mm-thick Carbon Fiber Reinforced Plastic (CFRP) plates surrounding the BGO Well, (iii) a layer of damping materials, and (iv) a plastic top piece with the same tapering as (i). The top cap, (i), is made of reinforced plastic Reny 1022F (polyamid MXD6 with glass powder; Mitsubishi Engineering Plastic Co.), which is easily machinable and has a coefficient of thermal expansion similar to the BGO crystals. The cap is glued on top of the BGO Well using an elastic epoxy (Konishi-bond MOS7; epoxy-silicon composite) to release the thermal stress. The top cap serves as an extension to the BGO Wells, and absorbs the stress concentrating on the end corner of the Well. The CFRP plates, (ii), are glued with epoxy resin Araldite AV138/HV998 (by Ciba Geigy) to both the BGO Well and component (i), and reinforce the Well rigidity against the lateral vibration. The component (iii), having a thickness of 2 mm, is made of an RTV silicon rubber and a damping rubber, arranged in mozaic pattern. The RTV rubber is necessary to prevent the layer from creeping under a continuous force. This composite damper is particularly effective for suppressing the lateral resonances of the Well, which occur in the range 150−1000 Hz. The top piece, (iv), is also made of Reny 1022F, and its tapered surface fits into a tapered mating structure in the lid of the HXD-S housing. This structure allows a precise positioning of the Well in the housing. The damping layer is sandwiched between, and glued to, these two Reny pieces.

The bottom part of the holding structure is of similar design as the top part, except that there is no components corresponding to (i) or (ii). Therefore, the damping materials are directly glued to the BGO bottom block. The conical surface of component (iv) fits in the conical hole in the bottom part of the HXD-S housing. By appropriately applying pressure through the top lid of HXD-S housing, the two (top and bottom) support structures hold the Well properly in both lateral and axial directions.

To collect the scintillation light effectively, we use two kind of reflectors. $BaSO_4$ powder is painted on every surface of the BGO crystals where the support structures are glued. The remaining surface with no paint is covered with two layers of 250 μm thick Gore-Tek sheet. These reflectors are selected by actually measuring their reflectivity.

To eliminate the units with mechanical defects, each unit went through a thermal cycle test, ranging from $-20°$C to $30°$C, after the support structure was glued.

3.3. The PMT Read Out of the Crystal Part

At the bottom end of the BGO crystal, a 2-inch ruggerdized PMT, R6231-07, from Hamamatsu Photonics is glued with $\sim$ 0.5 mm thick silicon compound KE108. A ring made of Reny is glued to the cylinder part of the BGO crystal, and a μ-metal tube with a length of 134.5 mm and thickness of 0.5 mm is fixed to the crystal using the ring. The μ-metal tube is used to hold the electronics part and shields the whole PMT from geomagnetism. The operating voltage of the PMT is set around 900 V.

We measured the light yield of each Well unit with the test electronics at the temperature $-20°$C. Figure 3 shows the a sample spectrum of the Well unit irradiated by 662 keV γ-rays from ^{137}Cs. The signal output of the PMT is fed to a pre-amplifier and then shaped by a shaping amplifier with 1 μsec filter, which is taken to be similar to that of the main shaping chain of the flight model electronics.[56] Among the 16 units used for flight, the FWHM resolution of the GSO peak ranges from 9.95 % to 10.21 %. The relative pulse hight of the BGO bottom part compared to that of the GSO ranges from 0.45 to 0.51, and that of the BGO well part ranges from 0.23 to 0.29. The positional difference of the light yield in the BGO well part within each unit is less than $\sim$ 4 %.

3.4. Fine Collimators and PIN Diodes

Fine collimators are made of 50 μm thick phosphor bronze sheet, arranged to form a 8×8 square channels of 3 mm wide and 300 mm long each. This limits the FOV of the HXD to $0°.57 \times 0°.57$ (FWHM) in the lower energy band. The fine collimator becomes transparent above $\sim$ 100 keV, approaching the larger FOV of $4.57° \times 4.57°$ (FWHM) defined by the BGO well.

Outer shell of the fine collimator is made by 200 μm thick phosphor bronze sheet. In the bottom of the fine collimator, the outer shell is extended by 14 mm to make room to accomodate a PIN diode assembly. The assembly has a dimension of 23.5 mm $\times$23.5 mm $\times$13.5 mm. Because the assembly is nearest to the PIN diodes and GSO, materials contaminated with little or no radio isotope are carefully selected. A chip of silicon PIN diode is glued on the assembly, which has a dimension of 21.5 mm $\times$ 21.5 mm $\times$ 2 mm. The photon collecting area of each diode is around 2.56 cm^2, depending on the reverse voltage of around 400 V. The bottom end of the fine collimeter is covered with alminized Kapton (see Fig.4).

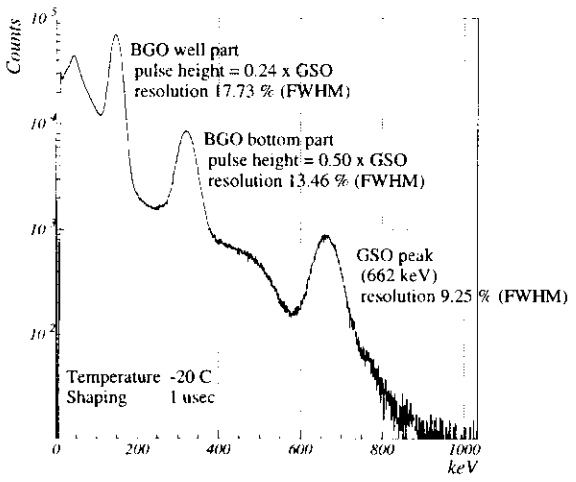

Figure 3. ^{137}Cs spectrum taken with a flight model Well unit. Note that the electronics are different from the flight ones, though the shaping time of 1 μsec is similar to that used in the flight electronics. Horizontal axis is energy in keV, calibrated to the GSO peak. The pulse height from the BGO bottom part and the BGO well part is 50 % and 24 % of that of GSO, respectively. Energy resolution of each peak is also shown in FWHM.

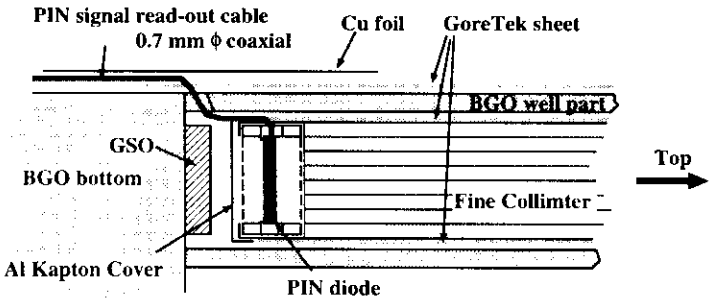

Figure 4. Schematic drawing of the signal read-out from the PIN diode.

Four fine collimators are inserted in each Well unit. They are wrapped with two layers of 250 μm thick GoreTek sheet to reflect the scintillation light of the BGO well. In addition, the thickness of the sheet is carefully measured and selected to fit the inner size of each well, to accurately align the fine collimators with BGO active collimator. The fine collimators are glue to the top cap.

The signal readout of the PIN diode is designed to reduce the electrical noise. This is important to lower the noise so that the lower energy of the HXD continues to those of the XIS and XRS. A 20 μm thick copper foil surrounds the BGO well around the PIN diodes to reduce the electric noise from outside. A coaxial cable from each diode assembly comes out from the BGO well through a tiny hole cut in the BGO side plate, and runs under the foil and then along the PMT, down to the pre-amplifier at the bottom of the unit. The fine collimators are electrically connected to the signal ground of the pre-amplifier.

The noise level of the PIN diode was measured after all the parts of the HXD-S are put together, using the flight model electronics. The achieved energy resolution at -20°C is around 3.5 keV (FWHM), and the threshold of $\sim$ 10 keV has been achieved. Figure 5 shows the spectrum of the 14.2 keV K-α line of Sr from radio isotope ^{88}Y, measured with the PIN diodes (see also § 7).

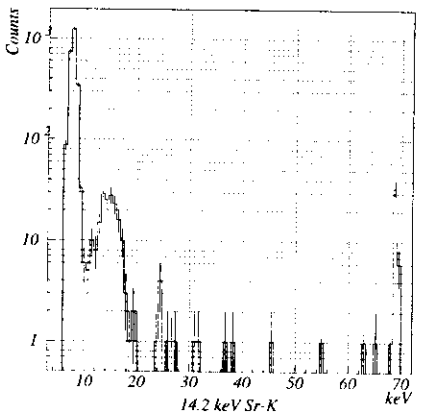

Figure 5. Spectrum of the 14.2 keV Sr K-α line measured with a PIN diode, in the pre-flight calibration. Temperature is set to -20°C. Electronics are of the flight model. We can see that $\sim$ 10 keV lower threshold is realized, bellow which the thermal and electrical noise dominate.

4. PRODUCTION OF THE ANTI UNIT

Anti units are made of thick BGO crystals having a large stopping power. There are 16 Anti-Side units and 4 Anti-Corner units in HXD-S (see Fig. 1). An Anti-Side unit consists 397 mm long BGO crystal part with support structure, and 144 mm long electronics plus PMT, and weighs 4.32 kg. An Anti-Corner unit is made of slightly slimmer crystal and the same PMT, and weighs 2.62 kg.

4.1. Support Structure of the Anti Unit

The support structure is basically the same as that of the Well unit. The Anti unit, however, has a wedge like shape for weight saving and the top part is very thin. It cannot hold itself against the severe mechanical vibrations. A thick cap made of Reny is therefore glued at the top. In addition, a box like structure made by $\sim$ 1.2 mm thick angles of CFRP is glued on three sides of the detector unit to support the crystal (see Fig.6).

As the Anti units act as active shields for the Well units, and also required a moderate energy resolution for monitoring the transient sources, the $BaSO_4$ reflector is painted on all the surfaces of the crystal, except around the PMT. The composite rubber layer is glued on the cap and the bottom of the crystal for vibration damping, just like the case of the Well units.

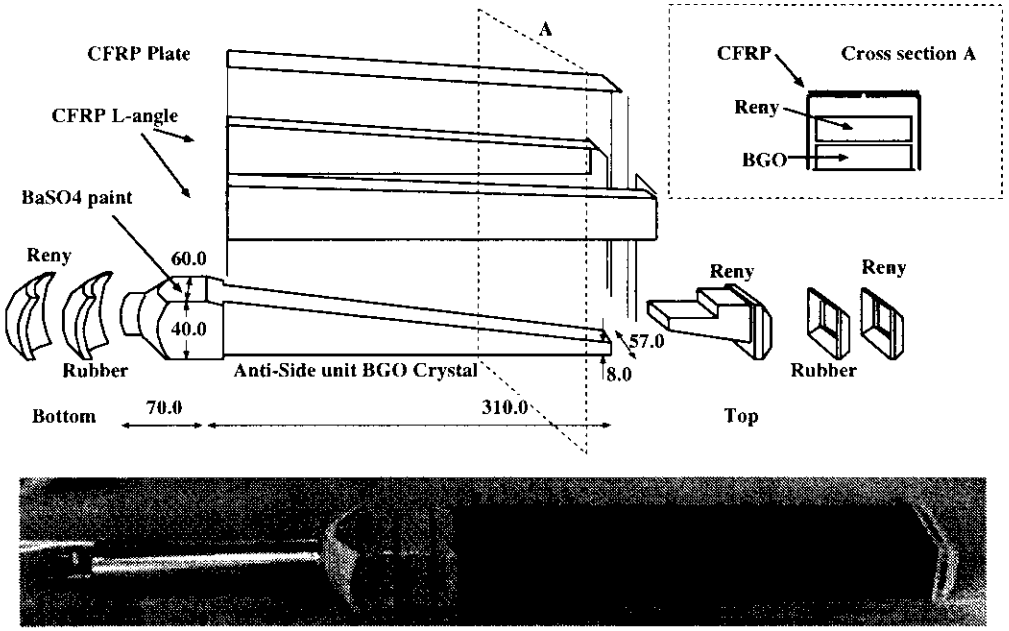

Figure 6. (*top*): Schematic drawing of Anti-Side unit. The BGO crystal, support structures made of CFRP, and holding structure made of Reny and rubber are shown. PMT assembly is mounted beneath the bottom part such as the Well unit. (*bottom*): Picture of a flight Anti-Side unit.

4.2. The PMT and the Performance Check

At the bottom part of the Anti unit, a $1\frac{1}{8}$-inch ruggerdized PMT, R3998-01, from Hamamatsu Photonics is glued with $\sim$ 0.5 mm thick silicon compound KE108. It is also surrounded by a μ-metal tube, and is operated with a high voltage around 800 V.

As the Anti unit has a wedge like shape, the positional dependence of the light collection efficiency is rather large. This lowers the energy resolution, which is measured to be $\sim$ 27 % for 662 keV at -20°C, when uniformly irradiated.

5. HXD-S HOUSING

5.1. Basic Structure of the Housing

The HXD-S housing is designed to hold the 36 detector units and align the 16 Well units with one another. It also has to protect the units from the mechanical environments, minimize temperature gradient among the units, and reduce electrical noise. These requirements should be realized within the limited space and weight allowed to the instrument.

The housing structure of HXD-S is basically made of three components: the top lid and the center body part made of CFRP, and the bottom structure made of Magnesium-alloy (see Fig. 7 *left*). CFRP is selected not only for its strength and light weight It also has a lower coefficient of thermal expansion than the BGO crystal, and will not stress the detectors once HXD-S is cooled to the operating temperature of -20°C in orbit. The top lid has 64 square openings matching the FOV of the Well units, and another thin (400μm) plate of CFRP is used to cover them for light protection. The total weight of the housing is 27.3 kg.

The electronics attached to the housing are high-voltage power supplies (HVs) for PMTs and PIN diodes mounted on the bottom structure, and the thermometers to measure the temperature of HXD-S. Cables for electrical connection to HXD-AE is placed below the HVs.

5.2. Holding Mechanism and Alignment of the Units

Each detector unit is held between the top lid and the bottom part of the housing. Holders made of Reny are glued to the top lid, while the housing bottom part has a tapered holes where the detector units sit in. The gap between the crystals of the adjacent detector units are as small as 4 mm, to ensure the effective active shielding.

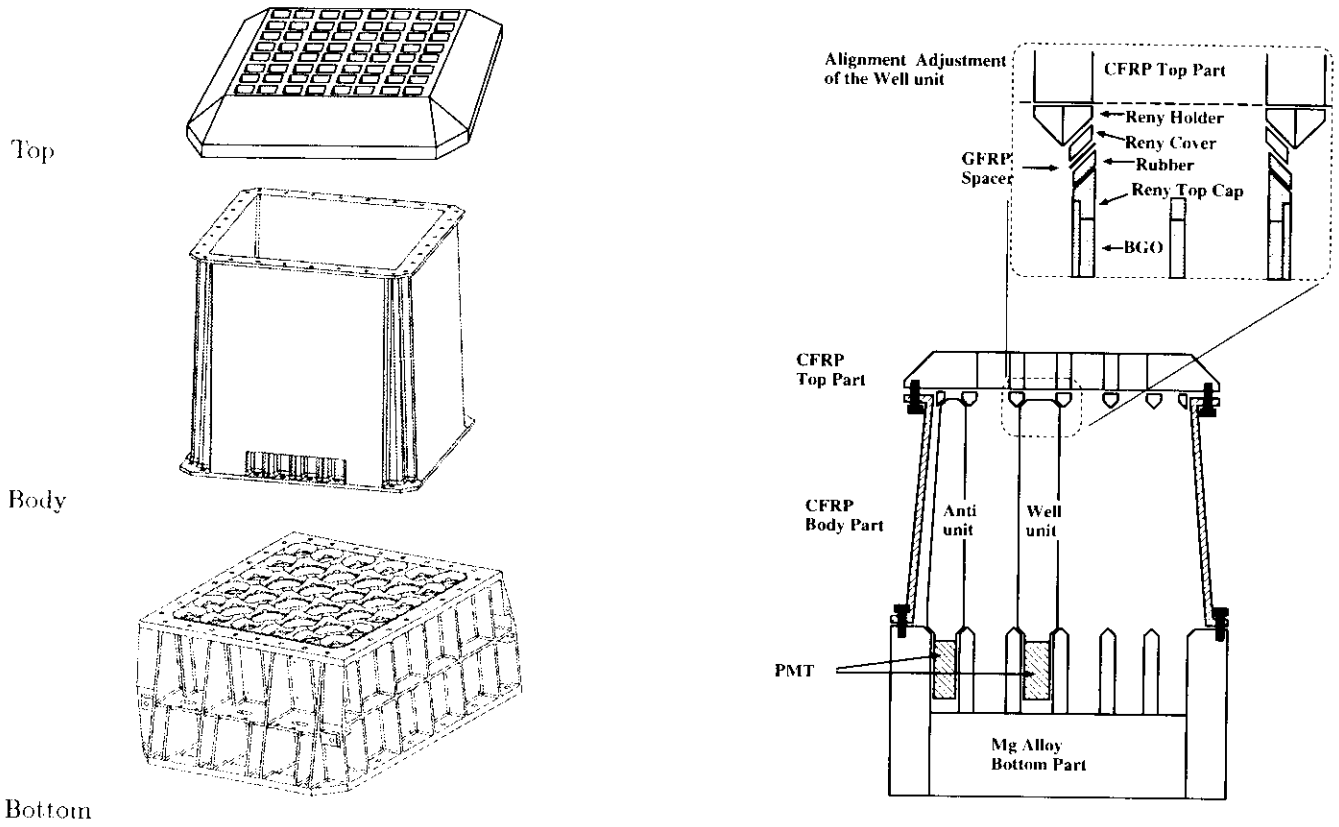

Figure 7. (*left*): The design of HXD-S housing. High voltage supply and other electronics are not shown. Top lid and body part are made of CFRP. The bottom part is made of Magnesium alloy. (*right*): Concept of holding the detector units and alignment of the Well unit. Units are held between the top lid and bottom part of the housing. All the detector units are produced to have the same height. In the Well unit, a shim made of Glass Fiber Reinforced Plastic (GFRP) is put between the Reny cover and the rubber, to adjust the alignment of the unit (in this case, to the right direction).

The detector units have been manufactured carefully, to attain a dimensional accuracy down to $\sim 100\mu$m. This is important for both alignment and protection against vibration. In addition, we adjusted the alignment of each Well unit within ~ 3 arcmin (see Fig.7 *right*).

5.3. Thermal Design

To achieve an operation temperature of -20 ± 5°C, HXD-S is mounted on a cold-plate, which in turn is mounted on the the lower deck of the spacecraft. The cold-plate is kept in low temperature via radiation cooling and also equipped with a heater to control its temperature.

The heat generated in HXD-S is ~ 17 W, half of which is from the HVs. Therefore the HVs are placed outside the Multi-Layer Insulator (MLI), thermally insulated from the main body of HXD-S, and radiatively coupled to the spacecraft. The remaining power is dissipated in the pre-amplifiers and PMT bleeders. In order to let these heat flow smoothly into the cold-plate, we used several techniques such as thermal bus bars, silicon rubbers with high heat conductivity, and so on. The thermal design if HXD-S has been verified in a thermal-vacuum test using the spacecraft thermal model. Total of 48 thermometers monitor the temperature in HXD-S.

5.4. High-voltage Power Supply

Twelve units of HV are mounted at the bottom part of the housing. Eight of them are for PMTs, producing ~ 800 V, and the other four are for PIN diodes, producing ~ 400 V. They are light-weight (70 g), highly stabilized (± 0.1 %) DC-DC converters with a high output current ($\leq 400\mu$A at 1 kV output) As mention in the last § 5.3., they are exposed to the spacecraft thermal environment.

The Well units are grouped into four, with respect to the gain of the crystal and the PMT. Anti units are also grouped in four in the same way, each having four Anti-Side units and one Corner-unit. Each group is supplied by a single HV. The power supply and the signal precessing at HXD-AE are also grouped to match that of the detector units.

5.5. Noise Reduction

The housing structure is made of CFRP and Magnesium alloy. Because both have high electric conductivity, they can shield the detectors from external electro-magnetic noise. The electric ground of the housing and that of the electronics therein are taken out separately, to reduce the noise in the HXD system.

Power lines and signal lines to HXD-S are handled in 24 groups, 16 for Well units, 4 for Anti units and 4 for controlling the HVs and temperature monitoring. They are connected through the connectors mounted beneath the HVs. To reduce the external common mode noise, ferrite cores are used for all signal lines.

6. FINAL CONFIGURATION OF THE HXD-S

HXD-S has finally been assembled in May of 1999. We performed mechanical tests, thermal test, and vacuum test to HXD-S. After these environmental verifications, the alignment of the 64 fine collimators were measured. Then HXD-S was connected to HXD-AE, and calibrations have been conducted in a thermostatic chamber at a temperature of $-20°C$.

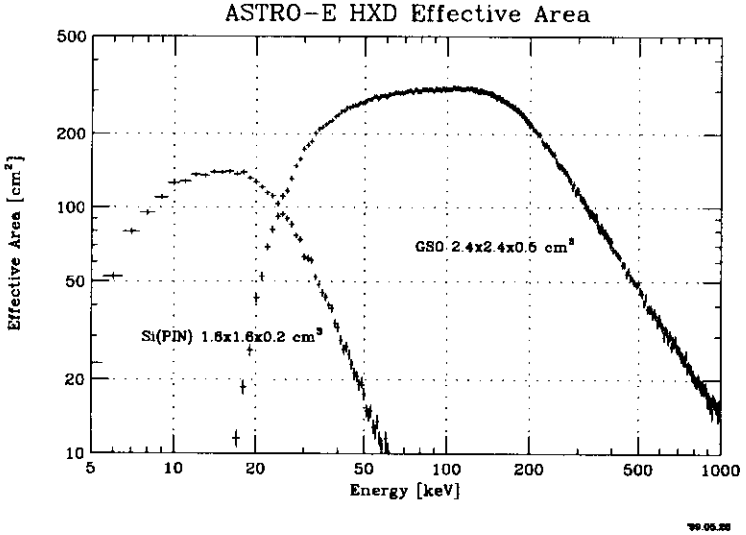

Figure 8. The effective area of the HXD. Note that the transmission of the fine collimator is assumed to be that of the ideal one. The mis-alignment of the collimators is estimated to reduce the effective area by about 10 %. Cut off around 10 keV is due to the cover plate made of 400 μm thick CFRP plate.

In Fig. 8, we show the effective area of the HXD, based on the latest calibration data. Fine collimator is assumed to be perfectly aligned in this figure. Then, the geometrical area of the PIN diode is 160 cm^2, and that of the GSO is 350 cm^2. We optically measured the alignment of the 64 fine collimators in HXD-S, and confirmed that they are aligned within 3.5′ (FWHM) accuracy. This assure an effective transparency of around 90 %. The results will be cross calibrated in orbit, using the Crab Nebula.

The room background level achieved in the pre-flight calibration is shown in Fig. 9. Background count is normalized by the detector effective area. Background levels of other hard X-ray experiments in orbit are shown together for comparison. We can see that the HXD has realized the lowest background level.

In the pre-flight calibration, we set the energy range of the PIN diode to 10 – 60 keV, and that of the GSO to 30 – 600 keV. The measured energy resolution is 3.5 keV (FWHM) for the PIN diode and $2.4 \times \sqrt{E(\mathrm{keV})}$ keV (FWHM) for the GSO. (see table 1).

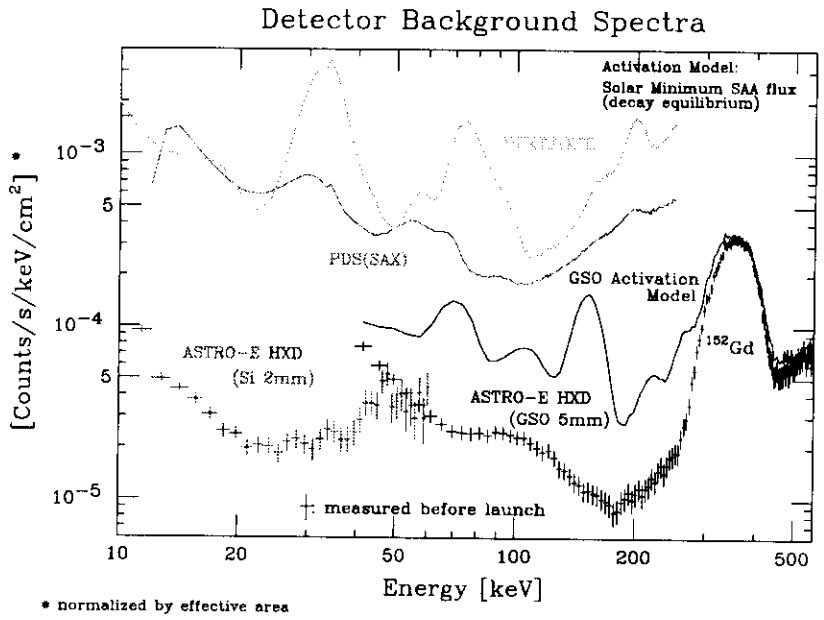

Figure 9. Background spectra acquired in the pre-flight calibration, normalized to the effective area of the detector. For the GSO scintillator, a background including the effects of expected in-orbit radio-activation is also shown[14].

7. SUMMARY

We have accomplished the fabrication of HXD-S, as well as HXD-AE and HXD-DE. They have successfully passed the environmental tests. A detailed pre-flight calibration confirm that the performance of the HXD meets the design goal of the experiment, including the threshold of $\sim$ 10 keV of the PIN diode, and the very low room background of $1-5 \times 10^{-5}$ counts sec^{-1} keV^{-1} cm^{-2}.

ACKNOWLEDGMENTS

The present work is supported by Fellowships of the Japan Society for Promotion of Science for Japanese Young Scientists, Grant-in-Aid for Science Research No. 05242101 and Grant-in-Aid for COE research No. 07CE2002 by the Ministry of Education, Culture and Science, Japan.

REFERENCES

1. Inoue, H. *Proc of the 11th Colloquium on UV and X-Ray Spectroscopy of Astrophysical and Laboratory Plasmas.* Universal Academy Press, (Tokyo,1995)
2. Ogawara, Y., et al.*proc. of IAU Symposium no. 188.*(Kyoto,1998)
3. Takahashi, T., et al. *Astron Nachr.* , 319, 3, pp.159 (1998)
4. Kamae, T., et al. *proc SPIE.*2806, 314 (1996)
5. Takahashi, T., et al. *proc SPIE.*3445, 155 (1998)
6. Tanihata, C., et al. in this volume.
7. GSO crystal, by Hitachi Chemical.
8. Takagi, K. and Fukazawa, T., *Appl. Phys. Lett.*, 42, 43 (1983)
9. Ishibashi, H., et al *IEEE Trans. Nucl. Sci.*, 36, 170 (1989)
10. Tsuchida, N., et al. *Nucl. Instr. Meth.*,A385, 290 (1996)
11. BGO crystal, by Crismatec.
12. Silicon PIN diode, by Hamamatsu Photonics.
13. Kaneda, H., et al. *proc SPIE.* 2518, 85 (1995)
14. Sugizaki, M., et al. *proc SPIE.* 3115, 244 (1997)
15. Kobayashi, M., et al., KEK Internal Report, 91-1 (1991)

16. Kokubun, M., et al. *IEEE Trans. Nucl. Sci.*,in press (1999)
17. Kataoka, J., et al. *proc SPIE* , 3445, 143 (1998)
18. Kaneda, H., Master Thesis, Dept. of Physics, Univ of Tokyo (1994)
19. Tamura, T., Master Thesis, Dept. of Physics, Univ of Tokyo (1995)
20. Iyomoto, N., Master Thesis, Dept. of Physics, Univ of Tokyo (1996)
21. Mizuno, T., Master Thesis, Dept. of Physics, Univ of Tokyo (1997)
22. Kubota, A., Master Thesis, Dept. of Physics, Univ of Tokyo (1998)
23. Nakazawa, K., Master Thesis, Dept. of Physics, Univ of Tokyo (1998)
24. Ota, N., Master Thesis, Dept. of Physics, Univ of Tokyo (1998)
25. Yamaoka, K., Master Thesis, Dept. of Physics, Univ of Tokyo (1998)
26. Matsumoto, Y., Master Thesis, Dept. of Physics, Univ of Tokyo (1999)

Preflight Performance of the Astro-E Hard X-ray Detector

C. Tanihata[a,b], J. Kataoka[a,b], T. Murakami[a], N. Ota[a,b], H. Ozawa[a,b], T. Takahashi[a,b], T. Tamura[a], Y. Uchiyama[a,b], S. Watanabe[a,b], K. Yamaoka[a,b], D. Yonetoku[a,e], Y. Ezoe[b], Y. Fukazawa[b], N. Isobe[b], N. Iyomoto[b], T. Kamae[b], M. Kokubun[b], J. Kotoku[b], A. Kubota[b], K. Makishima[b], Y. Matsumoto[b], T. Mizuno[b], K. Nakazawa[b], T. Onishi[b], M. Sugiho[b], I. Takahashi[b], M. Tanaka[b], M. Tashiro[b], Y. Terada[b], M. Nomachi[c], A. Yoshida[d], M. Hamaya[f], M. Horii[f], K. Taguchi[f], N. Morita[g], I. Odagi[g], K. Sato[g], Y. Tanaka[g], and K. Mori[h]

[a]Institute of Space and Astronautical Science (ISAS)
3-1-1, Yoshinodai, Sagamihara, Kanagawa, 229-8510, Japan

[b] Department of Physics, University of Tokyo
Hongo 7-3-1, Bunkyo-ku, Tokyo, 113-0033, Japan

[c]Research Center for Nuclear Physics, Osaka University
Mihogaoka, Ibaraki-shi, Osaka, 567-0047, Japan

[d]Institute of Physical and Chemical Research (RIKEN)
2-1 Hirosawa, Wako, Saitama, 351-0198, Japan

[e]Tokyo Institute of Technology (TITech)
2-12-1 Ohokayama, Meguro-ku, Tokyo, 152-8550

[f]Meisei Electric Company Ltd.
249-1 Moriya-Kou, Moriya, Kitasouma-gun, Ibaraki, 302-0115, Japan

[g]Fujitsu Ltd.
4-1-1 Kamikodanaka, Nakahara-ku, Kawasaki, Kanagawa, 211-8588, Japan

[h]Clear Pulse Company Ltd.
6-25-17, Chuo, Ohta, Tokyo, 143-0024, Japan

ABSTRACT

The Hard X-ray Detector (HXD) is one of the three experiments of the Astro-E mission, the fifth Japanese X-ray satellite devoted to studies of high energy phenomena in the universe in the X-ray to soft gamma-ray region.[1–3] Prepared for launch at the beginning of 2000 via the newly developed M-V launch vehicle of the Institute of Space and Astronautical Science, the Astro-E is to be thrown into a near-circular orbit of 550 km altitude , with an inclination of 31 degrees.

The flight model has been finished assembled this year, and we carried out various tests to verify the performance. We acquired the background spectrum at sea level, and confirmed that our system is operating effectively in reducing the background level. The HXD will observe photons in the energy range of 10-600 keV, and the calculations based on the preflight calibration suggest that the HXD will have the highest sensitivity ever achieved in this energy range. We also verified that our electronic system will maintain its performance against charged particle events expected in orbit.

Keywords: Hard X-ray Detector, Astro-E, space environment, detector backgrounds, electronic system

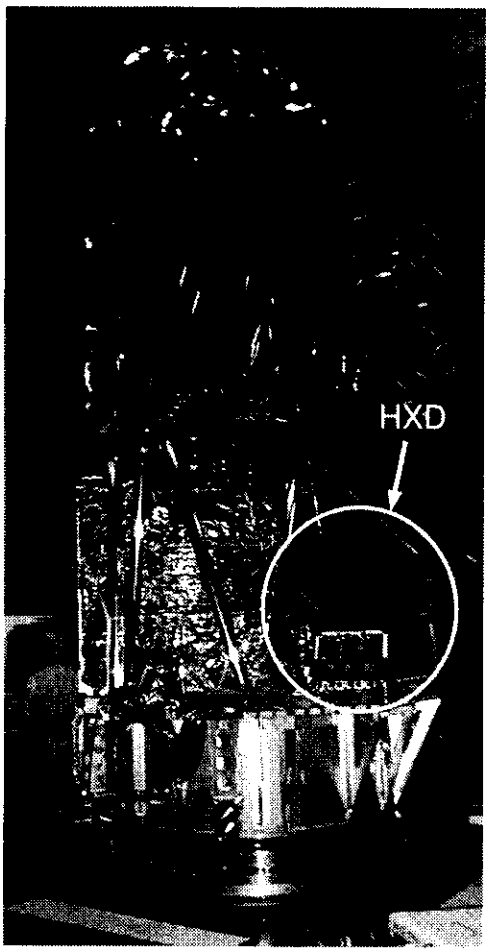

Figure 1. A picture of the HXD set onboard the Astro-E

1. INTRODUCTION

The difficulty of hard X-ray to gamma-ray spectroscopy is that the signal intensity from the source is usually weaker than detector backgrounds. The main causes of the background include diffuse gamma rays, radioactive nuclei due to the activation of the detector itself, and also cosmic rays such as protons and other heavy ions. Besides, Compton down scattering becomes dominant as energy becomes higher, which makes proper signals to appear as backgrounds in the lower energy.

Since the background level sets the limit of the sensitivity, the Hard X-ray Detector (HXD) prepared to be onboard Astro-E is designed to minimize them by its improved phoswich configuration.[1-7] In phoswich (acronym of PHOSphor sandWICH) counters, two crystals with different decay times are used for the detection part (faster decay time) and the shielding part (slower decay time), and both signals are extracted by a single photomultiplier. Our phoswich counter ensures a low background through the following techniques.

The main detection part of the phoswich counter in the HXD is a Gadolinium silicate crystal (GSO: $Gd_2SiO_5(Ce)$, 5mm thick) buried deep in the bottom of the Well-shape Bismuth germanate crystal (BGO: $Bi_4Ge_3O_{12}$). The improvement is that the BGO shield acts not only as an active shield but also as an active collimator, which narrows the field of view (FOV) without enlarging the amount of passive material. To cover the lower energy, we also add a Silicon PIN diode (2mm thick) in the Well, right above the GSO. (hereafter Well unit, for the combination of the phoswich counter and PIN diodes.) The total observation energy of the Well unit will range from 10-600 keV. The FOV of the Well unit is $4^\circ.6 \times 4^\circ.6$, and since the cosmic X-ray background (CXB) dominates the background in the low energy band, additional passive collimators made of phosphor bronze sheet (50μm thick) are placed inside the BGO wells. This provides a narrower FOV of $0^\circ.56 \times 0^\circ.56$ for the energies below $\sim$80 keV.

On the other hand, it had always been a serious problem for phoswich counters that the trigger rate for the electronics increases together with the detector volume. In the HXD, we increase the photon collecting area by placing individual units in a matrix. In this way, each unit will also act as an active shield of each other (Compound eye configuration[4-7]). We have 16 (4×4) Well units, and for the outermost units, we have 20 surrounding thick anti-coincidence counters made of BGO (hereafter Anti units). The total effective area of the GSO and PIN diodes will respectively be 350 cm^2 and 160 cm^2. (see Nakazawa et al in this proceeding for figures and further description of the detector)

In section 2, we will first describe the data flow in the HXD, and also the selections to be performed against each trigger events. The performance of the flight model, assembled this year is reported in section 3 and 4. A picture of the flight-model HXD set onboard the satellite during the compatibility test is shown in figure 1.

2. DATA FLOW IN THE HXD

A block diagram of the onboard data processing system is shown in figure 2. The HXD is composed of the sensor part (HXD-S), the analog electronic system (HXD-AE), and the digital electronic system (HXD-DE). HXD-AE receives the analog signal from HXD-S, selects the proper events, and sends them to HXD-DE through the DMA Buffers. HXD-DE then formats the data packets to send them down to ground via the satellite data processor (DP). All the power are supplied from a power-supply unit called HXD-PSU.[20,21]

Looking further in HXD-AE, it consists of one control board (ACU) and 8 signal processing boards. The latter is broken into two types, 4 Well Processing Unit (WPU) boards for the Well units, and 4 Transient Processing Unit (TPU) boards for the Anti units. While the Well units acquire the data from the target source, the Anti units have the function of monitoring transient sources, and also gamma-ray bursts. The ACU is provided power from HXD-PSU, and controls the power lines of the electronic boards and also the power-supplies of HXD-S. It also monitors the House Keeping (HK) data, such as the high voltage values or temperatures of the scintillators and photomultiplier tubes.

Each WPU and TPU respectively handles 4 Well units and 5 Anti units. As shown in the figure, all WPU/TPU and ACU boards are connected to the backplane of the AE-box. In order to reject all the Compton events in the compound eye configuration of the HXD, it is important for each unit to be informed of the hit pattern of the other 35 units. The backplane is used to place the hit pattern bus, where the information of hits of all units are connected. Besides the hit pattern information, other lines, such as power-lines and clock-lines also run through the backplane. Further details of the electronics is described elsewhere.[21,23]

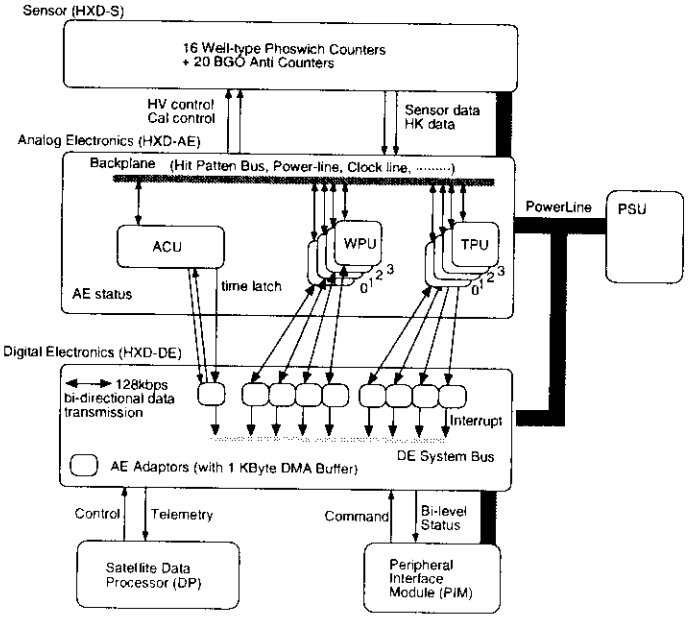

Figure 2. Block diagram of the data processing system of the HXD

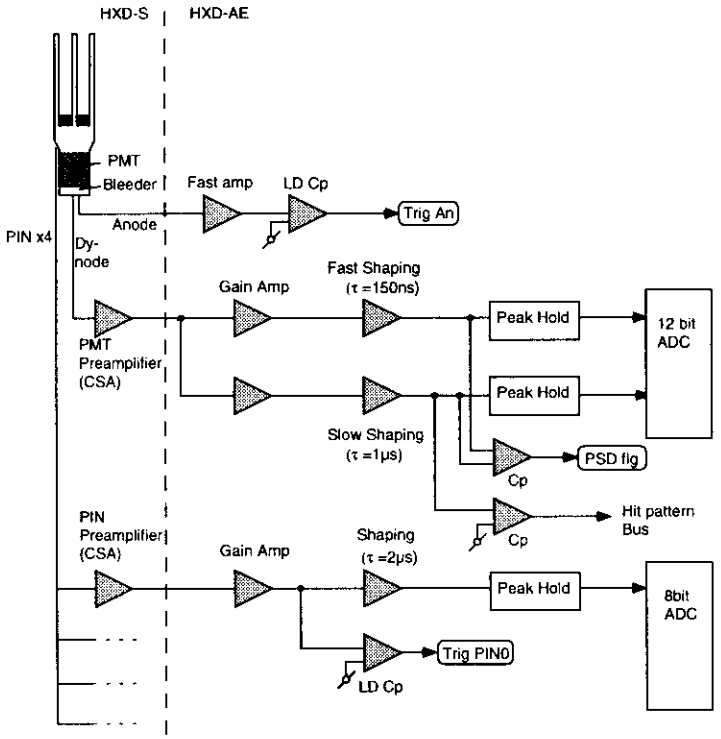

Figure 3. The signal flow of the Well unit. A pair of anode and dynode signal from the photomultiplier and 4 pin diode signals are processed in one unit.

2.1. Signal Processing of the Well unit

From a single Well unit, 6 channels of signals are extracted: 1 set of dynode and anode signal from the photomultiplier tube, and 4 PIN diode signals. The dynode and PIN signals are first processed by the preamplifier mounted in the housing of HXD-S, and then sent to the WPU modules in HXD-AE. Since the Well unit is operated in self-trigger mode, the signal to issue the peak hold gate must be generated as quickly as possible, especially for the GSO signals having a decay time as small as ~100 ns. This is the reason of extracting the anode and last dynode signal separately from the photomultiplier tube.

The signal flow of the Well unit is shown in figure 3. The anode signal is fed directly to a fast amplifier in HXD-AE to generate the trigger signals. Unlike the charge sensitive amplifier of the dynode signal, the anode amplifier just simply amplifies the current from the photomultiplier. The pulse width is shorter this way, which is required in generating fast pre-trigger signals. This also has a special meaning that the pulse height of a BGO signal becomes smaller than a GSO signal of same amount of light yield. This is due to the difference of the decay times, and is a great advantage in our configuration, where we want to reject all the BGO events. On the other hand, the preamplifier output generated from the dynode signal is split into two shaping chains with different time constants: 150 ns (fast shaping) and 1000 ns (slow shaping). Each of the shaped signal is then peak held (activated by the trigger signals) and sent to the Analog to Digital Converters (ADCs).

Since the decay time of the GSO and BGO are different (122 ns for GSO and 706 ns for BGO; both at $-20°C$[12]), the ratio of the fast and slow shaping pulse heights will differ between GSO and BGO. By the fast shaping, only the first portion of the charge is integrated for BGO, while the GSO signal is fully integrated. On the other hand in the slow shaping, almost all the charge is integrated for both crystals. Although the fast shaping output is still slightly lower than the slow shaping output for GSO signals, we can adjust the gain so as to discriminate the GSO and BGO events by comparing the fast and slow pulse heights by a comparator. This is called the double integration method for Pulse Shape Discrimination (PSD). A waveform of the fast and slow shaping output for a GSO and BGO signal is shown in figure 4.

The slow shaper output is also fed into a comparator to generate the Hit Pattern signal. This is the signal sent

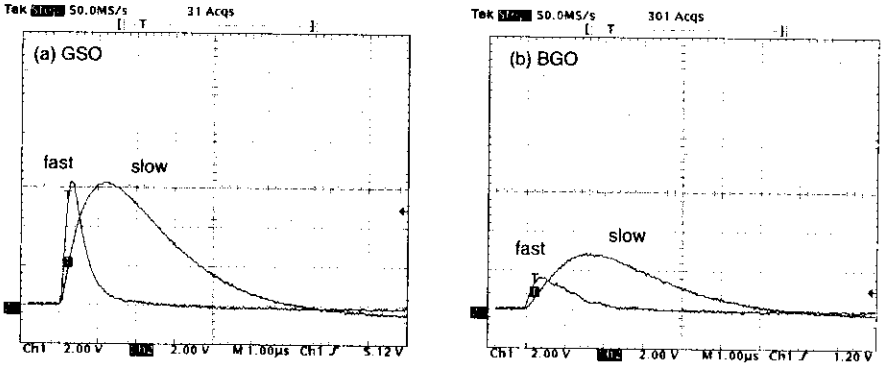

Figure 4. A waveform of the output of the fast and slow shaping for a (a)GSO and (b)BGO signals.

to the Hit Pattern bus.

2.2. Event Selection

Since both the GSO and BGO signals are extracted from a single photomultiplier, and because of the large volume of the active shielding, the trigger rate for the analog system is expected to be very high, as much as several kHz. Thus we must be able to effectively select only the events which deposit all of their energies in the GSO crystal, and also reject all the events that have a possibility of misreading in the pulse height. We will summarize the event selection at the end of this chaper.

Pulse Shape Discrimination (PSD) As described in the previous section, this discriminates the GSO and BGO events by comparing the pulse height of the fast and slow shapings. This rejects the BGO events and also the Compton scatterd events which hit both the GSO and BGO in the same unit.

Hit Pattern Selection While the PSD technique rejects the BGO signals in its own unit, the function of the Hit Pattern Selection is to reject the Compton scattered events which hit different units. The information of the hits of all 36 units (16 Well units and 20 Anti units) is latched every time the Well event is acquired. Although all information of 36 units can be used, the most dominant Compton scattering component is the events scattered with the adjacent units in the energy range of ~600 keV. Considering also that using all units for anticoincidence will increase accidental rejection, several types of rejection patterns can be considered. The most adequate is to refer 4 adjacents units, or 8 surrounding units. The selection pattern can be selected by onboard software.

Double Pulse Rejection Counting from the activation of the fast anode trigger, it takes 9.8 μsec till the AD conversion is complete. Since the counting rate in orbit is assumed to be at most 10 kHz, the piled-up events cannot be neglected. We mounted a double pulse detection circuit,[22] and the result of judgement is included in the Well event data.

3. PERFORMANCE OF THE FLIGHT MODEL

In order to acquire the best performance, the HXD is designed to operate at low temperature, $-20°C$. This will lower the leakage current of the PIN diodes, and thus improve the energy resolution. The resolution of the scintillators will also be improved due to increasing light yield.[12] To test the performance of the flight-model HXD, we set HXD-S in a thermostatic chamber with the temperature set at $-20°C$. The signals were extracted to the flight-model HXD-AE through a 4 m cable, similar to those used onboard the satellite, and data acquisition was done by a prototype model of the digital electronics (HXD-DE).

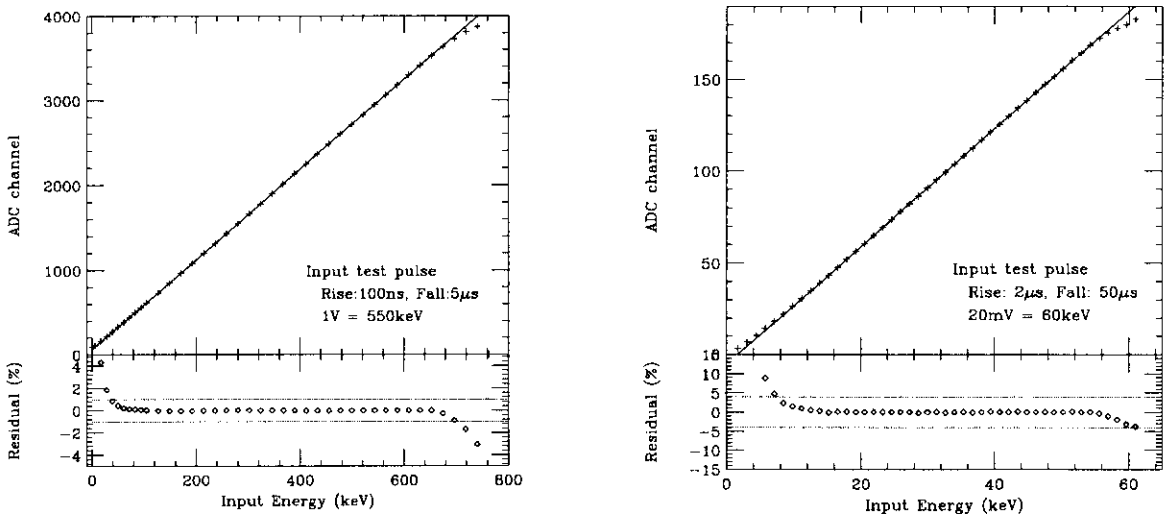

(a) Slow shaping for the phoswich counters

(b) Shaping for the PIN diodes

Figure 5. The linearity plot of the electronics acquired by inputting a test pulse in to HXD-AE. The linearity of the preamplifier is not included. The commandable gain of the amplifier was set at the default value.

3.1. Linearity of the Electronics

Before acquiring the data from the sensor, we measured the linearity of the electronics by inputing a test pulse into HXD-AE. The measured pulse height linearity and residuals are plotted in figure 5. The horizontal axis is the energy converted from the pulse height of the test pulse. For conversion, we used the typical value of energy to preamplifier output voltage, 550 keV = 1 V for the phoswich counter, and 60 keV = 20 mV for the PIN diodes. The dotted line in the residual plot shows our definition of the 'linear region', that is ±1% for the phoswich counter,[13] and ± 4% for the PIN diodes.[14] It is less strict for the PIN diodes because the dynamic range is smaller, and thus the number of ADC channels is smaller. (4096 channels for the phoswich counter, and 256 channels for the PIN diodes.)

We can see that the linear region is 40-700 keV for the photomultiplier, and 7-60 keV for the PIN diodes. The upper limit indicates the saturation of the shaper, while the lower limit results from the linearity of the peak hold circuit. Thus we must remind that the 'linear energy region' can be shifted by selecting the commandable gain of the shaping chain. According to the results, we made a look-up table for correcting the ADC channel to energy, including the lower and higher energy regions where the output starts to deviate from linear.

3.2. The Background Spectrum

As written in the introduction, in hard-X ray to gamma-ray spectroscopy, it is most important that the background level is kept low. Thus, we first measured the background spectrum at the sea level and verified the performance of each event selection as well.

3.2.1. Selection by Pulse Shape Discrimination

Figure 6(a) shows the acquired background spectrum of a typical Well unit in a fast-slow plane, where the vertical and horizontal axes represents the fast and slow shaping pulse height. In this way, we can see two branches with different inclination, demonstrating the separation of GSO and BGO. The events between the two branches are the Compton scattered events, whose time constant is a mixture of the two. The events selected by PSD is shown in figure 6(b). We can see that all the BGO and Compton events are effectively rejected. Below the GSO branch, we can see a narrow branch. Because of the very fast time constant, they are thought to be due to Cherenkov light generated in the glass of the photomultiplier. The total counts in this narrow branch is 5 - 10% of the GSO counts, and we will have to treat these events carefully.

Figure 7 is the energy spectrum (equivalent to the horizontal projection of the spectrum in figure 6) demonstrating the performance of the PSD. The top panel represents the total background energy spectrum together with the

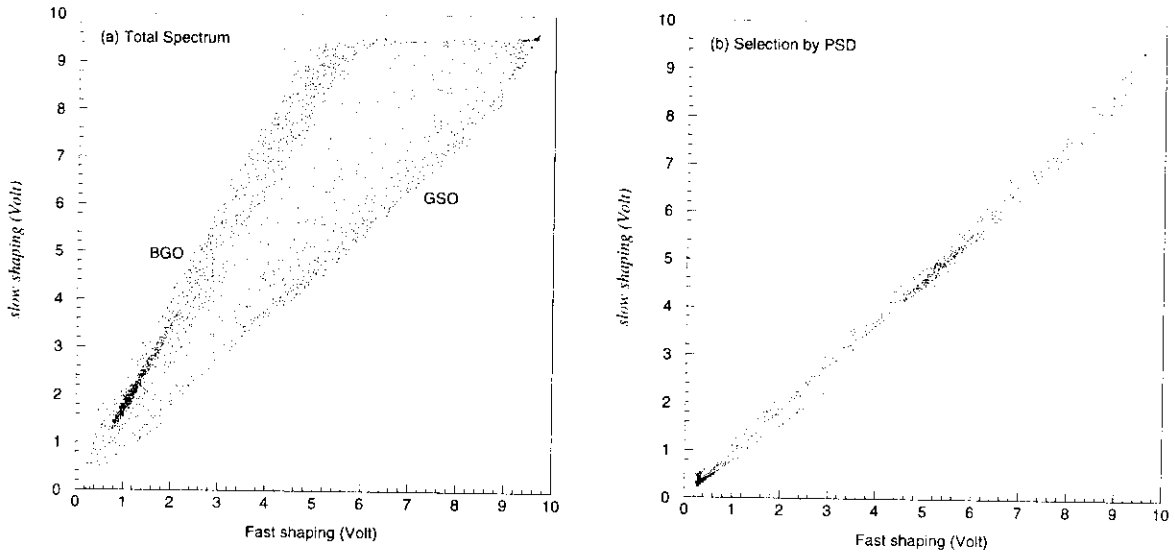

Figure 6. The effect of the Pulse Shape Discrimination (PSD) on the GSO background spectrum in a fast-slow plane of a typical Well unit. (a) Total spectrum. (b) The events selected by PSD.

spectrum after the selection: the latter can hardly be seen, indicating that the spectrum is dominated by the BGO and Compton events. The bottom panel shows the enlargement of the selected GSO spectrum.

In the GSO selected spectrum (figure 7 bottom), a peak around 360 keV is seen. This is due to the intrinsic radioactivity of ^{152}Gd in the GSO crystal (abundance 0.2%, 2.20 MeV α-decay, half-life 1.08×10^{14} year).[6,16] This has been known as the most dominant background at this energy. The total number of the GSO signal was 1.16% of the total trigger signal, and the clear presence of the Gd peak in the selected spectrum shows that the PSD filtering effectively suppresses the BGO and Compton signals.

3.2.2. Selection by Hit Pattern

Figure 8 shows the performance of the Hit Pattern selection for GSO, and also for the PIN diodes. The three lines indicate the spectrum selected by PSD (top), after further applying the Hit Pattern selection by 4 adjacent units (middle), and that using 8 surrounding units (bottom). For the PIN diodes, we also rejected the events which hit the BGO or GSO in its own Well unit. We can see that the Hit pattern selection effectively lowers the background levels, by keeping the flux of the intrinsic Gd peak almost unchanged. We can also see that using all 8 surrounding units for rejection further improves the background level. However, increasing the number of units will cause larger numbers of accidental rejection, which is equivalent to deadtime increase.

We will summarize the selected counts by each selection stage in the energy range of 30-600 keV for the phoswich counter and 10-60 keV for the PIN diodes in table 1. For the phoswich counters, we can see that 2.7% of the total counts is selected by PSD, and 57% of the selected events are further selected by hit pattern. On the otherhand, concerning the counts in the Gd peak, which is known to be intrinsic, only 2.5% was rejected by hit pattern. This indicates that the hit pattern is effectively rejecting only the Compton events, and does not degrade the signal acceptance.

The resulting background level at the sea level was $\sim 2\times10^{-5}$ cts cm^{-2}s^{-1}keV^{-1}at 100 keV, and $\sim 7\times10^{-6}$ cts cm^{-2}s^{-1}keV^{-1}at 200 keV for the phoswich counters, and $\sim 1\times10^{-5}$ cts cm^{-2}s^{-1}keV^{-1}at 30 keV for the PIN diodes. This is the lowest background level we have reached through out our development, including the balloon experiments.[7] This confirms that our system is operating as expected in lowering the background level.

	phoswich counter (%)	PIN (%)
total count	1281646 (100 %)	19214 (100 %)
PSD selection	34308 (2.68 %)	-
HP selection by adjacent 4 units	19573 (1.53 %)	12326 (64.1%)
HP selection by surrounding 8 units	18165 (1.42%)	11961 (62.2%)

Table 1. The selected counts in each selection steps for the background spectrum for the GSO and PIN events.

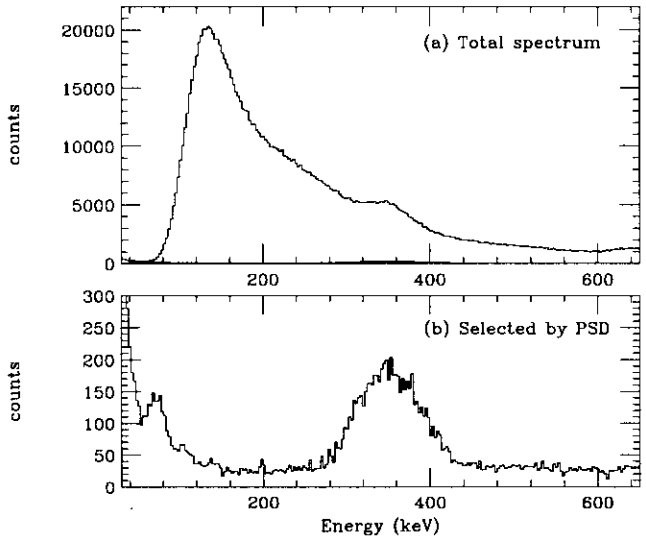

Figure 7. The pulse height spectrum of the GSO background data. (a) The total spectrum before (the upper curve) and after (the lower curve) the PSD selection. The latter can hardly be seen. (b) Enlargement of the selected GSO spectrum.

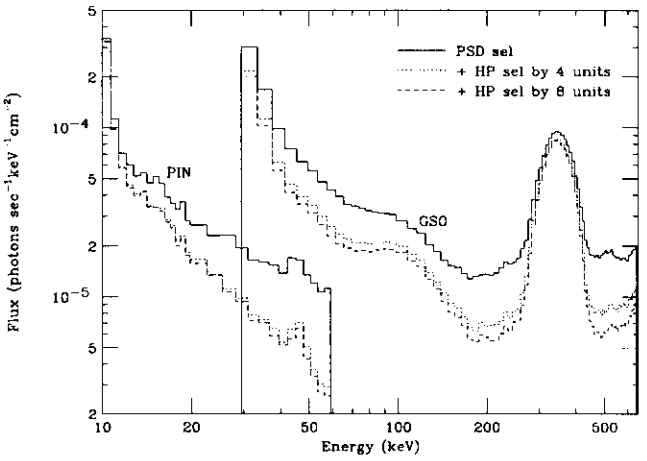

Figure 8. The effect of the Hit Pattern selection on the background spectrum. The solid line represents the spectrum selected by PSD, and the dotted line represents the spectrum after further applying the Hit Pattern. The difference in using 4 adjacent or 8 surrounding units for rejection is also plotted.

3.2.3. The Expected Background Level and Sensitivity

In orbit, the background level is expected to increase because of the radio-activation due to charged particles penetrating through the scintillators. Figure 9 represents the expected background specrum in orbit. The activation was simulated based on experiments of irradiating the scintillators by energetic particle beams, and the proton flux in the orbit of 550 km altitude at solar minimum was assumed.[16] From the expected background level, we can roughly estimate the detection limit of the HXD.

The sensitivity of a detector for a continuum spectrum is determined by the fluctuation of the background [b(E) cts $cm^{-2}s^{-1}keV^{-1}$] at a certain energy range [center E(keV); bin width ΔE]. The intensity necessary for a detection in a 3σ significance by a T_S sec observation can be written as

$$S(E) = \frac{3}{\eta(E)}\sqrt{\frac{2b(E)}{A\Delta E T_S}}, \tag{1}$$

where A and $\eta(E)$ stands for the geometric area and the full peak efficiency of the detector. By adopting the expected background level and $\Delta E/E = 0.5$ for the bin width of the energy spectrum, the detection limit can be calculated as in figure 10(a). Similarily, the sensitivity for line emission can be written as

$$S(E) = \frac{3}{\eta(E)}\sqrt{\frac{2b(E)\delta E}{AT_S}}, \tag{2}$$

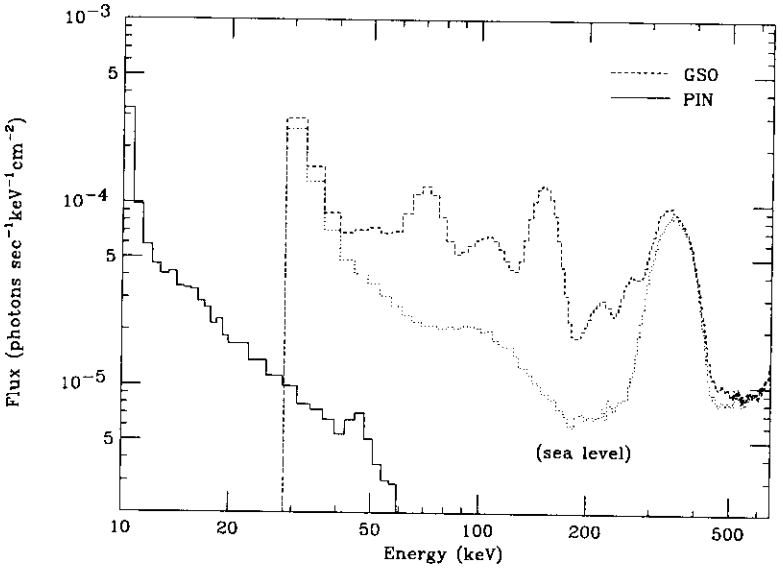

Figure 9. The expected background level in orbit. The solid and dotted line respectively represents the spectrum of the PIN diodes and GSO. The lower line in the GSO spectrum represents the background level at sea level taken in the laboratory.

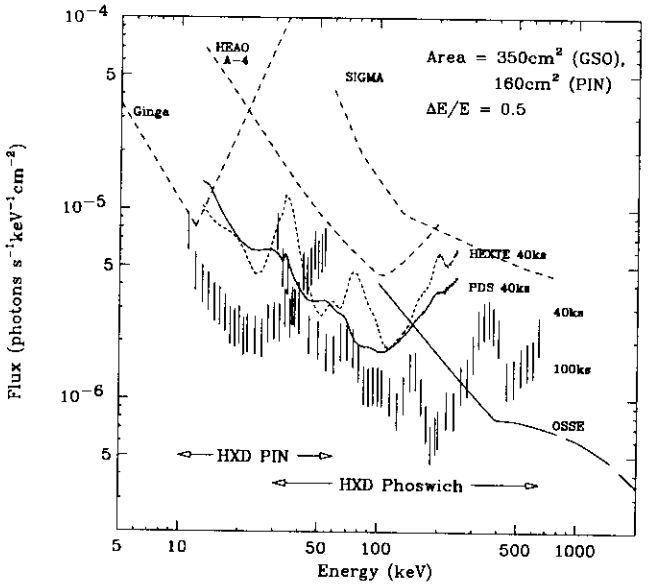

(a) Continuum Components

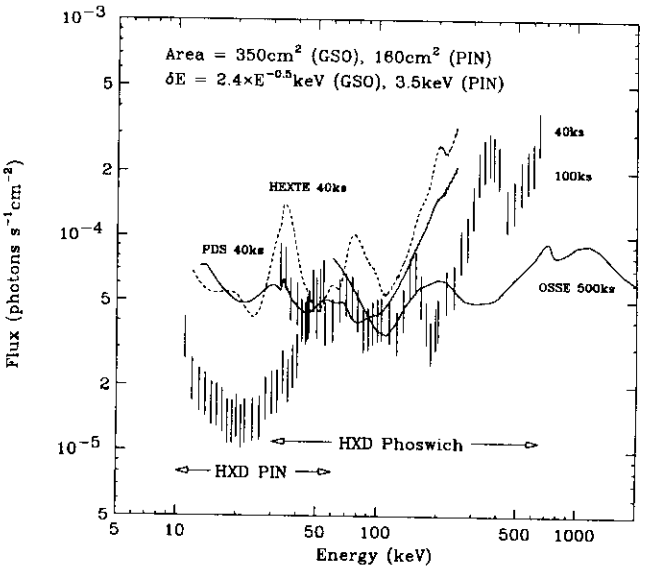

(a) Line Components

Figure 10. The expected sensitivity of the HXD in orbit for the (a) continuum and (b) line components

where δE stands for the resolution of the detector. The calculated sensitivity is plotted in figure 10(b). We also plotted the sensitivity of HEXTE onboard *XTE* and PDS onboard *BeppoSAX*, calculated in the same way. We can see that the HXD has the highest sensitivity in the energy range of 10-300 keV.

In the HXD, instead of rocking observation, we plan to perform background subtraction by modeling the background, as was done in the LAC detector in Ginga satellite.[8] Thus the sensitivity is to depend on the accuracy of the modeling.

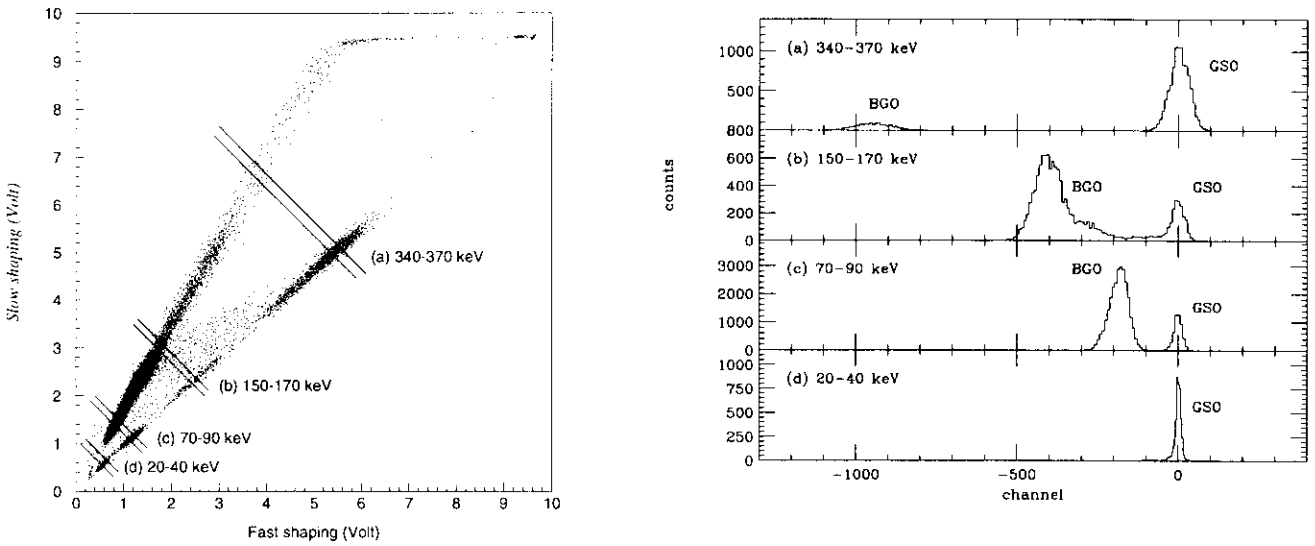

Figure 11. The separation of the GSO and BGO at different energies.

3.3. The Spectrum of Line γ-rays

3.3.1. The Performance of the PSD using Lines

As in the previous section, the PSD technique is the key in selecting the pure GSO events. However, since the GSO and BGO branches have a finite widths, they become closer as the energy lowers, and may start to mix with each other. Here, we will examine the separation of BGO and GSO branches on the fast-slow plane line γ-rays. Figure 11 is the spectrum on a fast-slow plane obtained by irradiating a ^{133}Ba isotope, which emit monochromatic γ-rays at 31.0 keV, 35.0 keV, 81.0 keV, 303 keV, and 356 keV. We can see 4 dark points in the GSO branch, representing each lines from the isotope.

To study the separation in different energies, we cut the spectrum with a line perpendicular to the GSO line, as in the left panel. The right panel shows the projection on to the perpendicular line. The peak on the left is the BGO peak, and we can see that two peaks approaching each other as the energy lowers. However at the lowest energy, only the GSO peak is present. This is the effect of the fast amplifier for the anode signal which makes the threshold level higher for the BGO events (section 2.1).

3.3.2. The Resolution

For preflight calibration perpose, we acquired the line spectra using several radioacitive isotopes. The isotopes we used are listed in table 2. We did the same event selection as the background data, that is, selection by PSD, and also Hit Pattern. Events that hit the shielding part are suppressed, and the remaining are those which deposited all its energy in the main detection part (GSO or PIN). We will show the spectra of lines from different isotopes in figure 12. Note that the 31 keV Kα line of the ^{133}Ba is clearly seen by GSO. The spectrum acquired by the PIN diodes are also shown in the same figure.

The energy resolutions for the PIN diode and GSO of a typical unit is summarized in table 2. We verified that the resolution of the PIN detectors meets our original goals, 3.5 keV at all energy.

3.4. The Power Consumption

It is important that all the elements satisfy the strict constraints due to space environments such as space, power, and also reliability of each parts. We summarize the final electric current and power consumption of the HXD in table 3.

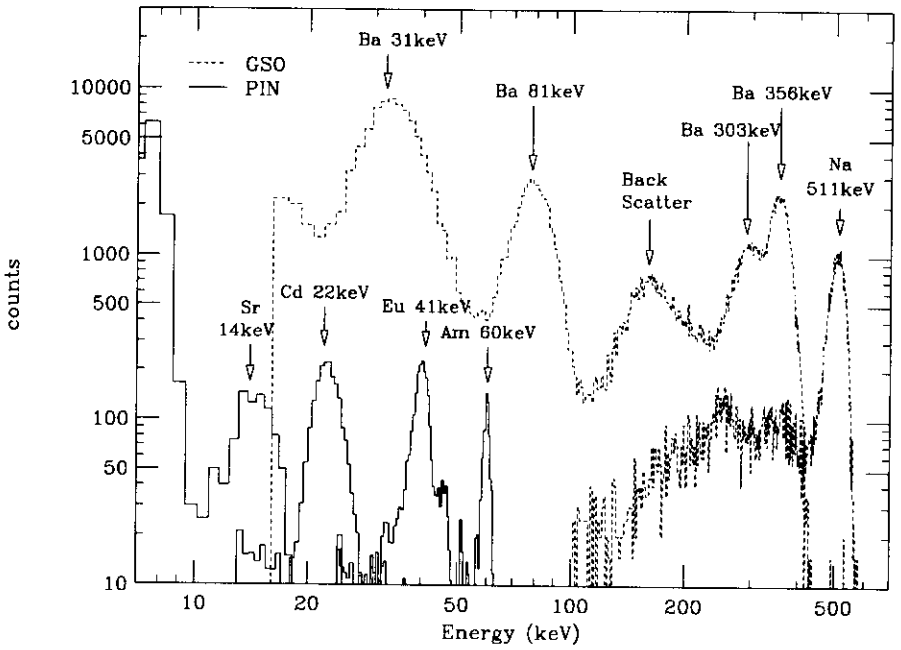

Figure 12. The energy spectra of the the HXD for γ-ray lines. The dotted line represents the GSO spectra irradiated by ^{133}Ba and ^{22}Na , and the solid line represents the PIN spectra irradiated by ^{109}Cd , ^{152}Eu , and ^{241}Am .

Table 2. The energy resolution for the γ-ray lines measured at $-20°$C by the phoswich counter.

Isotope	Energy (keV)	resolution(FWHM) by PIN (keV)	resolution(FWHM) by GSO (%)
^{109}Cd	22	3.6 ± 0.1	-
^{133}Ba	31.5	3.6 ± 0.1	-
^{152}Eu	41.1	3.5 ± 0.1	30.5 ± 0.6
^{241}Am	59.5	3.5 ± 0.6	28.5 ± 0.4
^{133}Ba	81	-	23.0 ± 1.3
^{152}Eu	122	-	18.8 ± 0.5
^{152}Eu	344	-	12.3 ± 0.2
^{22}Na	511	-	9.8 ± 0.2

	+12VA	-12VA	+5VA	+5VD	-5VA	total
HXD-S (mA)	920	90	43	0	120	
(W)	11.0	1.1	0.2	0.0	0.6	12.9
HXD-AE (mA)	1100	116	1100	560	986	
(W)	13.2	1.4	5.5	2.8	4.9	27.8
HXD-DE(mA)	3.0	0.0	0.0	1020	0.0	
(W)	0.036	0.0	0.0	5.1	0.0	5.1
S+AE+DE (mA)	2023	206	1143	1580	1106	
(W)	24.3	2.5	5.7	7.9	5.5	45.9

Table 3. The electric current and power consumption of the HXD

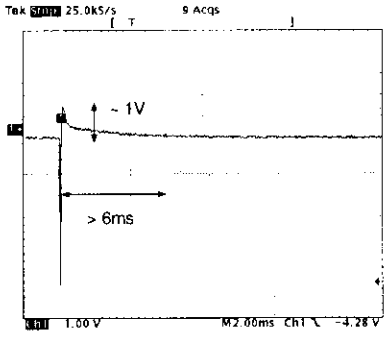

Figure 13. The preamplifier output for a 100 MeV deposit pulse using the original bleeder. The 100 MeV signal is simulated by an light pulser, and we can see that the recovery time was more than 6 ms.

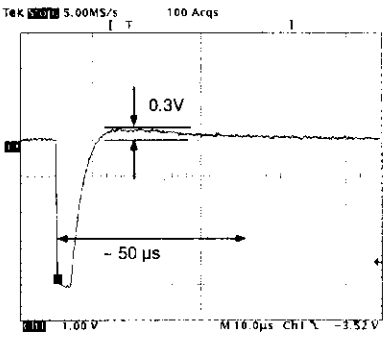

Figure 14. The preamplifier output for a 100 MeV pulse using the improved circuit (see Appendix). The recovery time is reduced to ~50 μs.

4. STABILITY OF THE ELCTRONICS AGAINST CHARGED PARTICLES

As written in previous sections, the trigger rate for the analog system in the Hard X-ray Detector is expected to be as much as several kHz. Charged particles are also a big matter. These include geomagneticaly trapped particles (mainly protons) and primary cosmic rays, and because the energy loss of a charged particle is proportional to the density and size of the detector, it becomes critical for the HXD utilizing a large and heavy scintillator for active shielding. The energy loss at the detector is estimated to be typically ~100 MeV, which is 3 to 5 orders of magnitude larger than the target energy. This is well above the saturation level of the amplifying system, and a long electronic recovery time would affect the following signals.

By the trigger logic, we inhibit the following triggers until the circuit has fully recovered to the initial state, so as to acquire only the events that are not affected by charged particles.[21] However, if the recovery time were too long, the deadtime caused by them would result to be long. Problems of large deadtime caused by charged particles have also been reported from detectors on earlier satellites.[18,19]

Thus it was premise to take these effects into account from the designing phase of the analog electronics. In order to make it strong for large pulses and also for high counting rates, it is most important to make the system to recover quickly for each signal. It is also important to do these measures from the very front-end of the signal processing chain.

Considering the requirements above, we designed the front-end electronics of the phoswich counter with a great care. We first attempted to understand the behavior of the circuits during the recovery, and then searched for the design to minimize the effect. In this chapter, we will show the stability of our electronics against charged particle events, and also against high counting rates.

4.1. The Phoswich Counters

4.1.1. Tests by Simulated Pulses

In order to shorten the recovery time of the signal from the phoswich counters, we studied the design of the voltage devider of the photomultiplier (bleeder) together with the preamplifier. Figure 13 shows the waveform of the preamplifier output of a 100 MeV deposit signal using our first design front-end electronics. For all the waveform of 100 MeV deposit signal shown in this paper, we utilized a light pulser made of an ^{241}Am source encapsulated in a small NaI(Tl) scintillator. The 5.486 MeV α-particle from the ^{241}Am is absorbed by the NaI, and since the light yield of NaI is large, we can easily simulate a 100 MeV-like signal by raising the high voltage of the photomultiplier. We can see that the it took more than ~6 ms to recover to the initial level. Since the expected counting rate of charged particles are ~200 Hz at most, this would result in 70 % deadtime. The recovery time was improved to ~50 μs using the improved circuit. The waveform is shown in figure 14. Details of the bleeder design is written in the Appendix.

In order to verify the tolerance of the electronics of the phoswich counters against large pulses, we used a Light Emitting Diode (LED) to inject a large light pulse into the photomultiplier tube. We can achieve a pulse with the

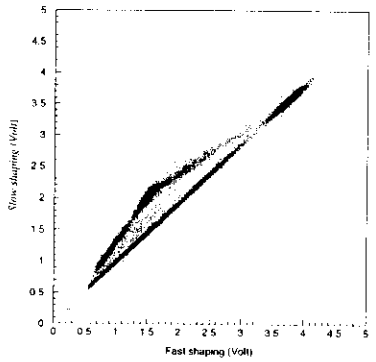

(a) Cs only (1 kHz)

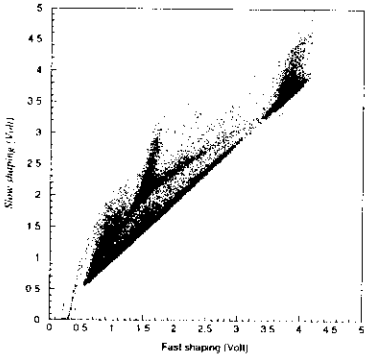

(b) Cs + 200 Hz LED
(Original circuit)

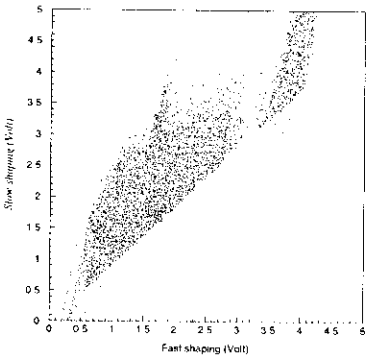

(c) Cs + 1 kHz LED
(Original circuit)

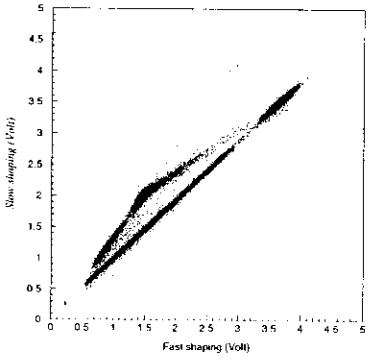

(d) Cs + 200 Hz LED
(Improved circuit)

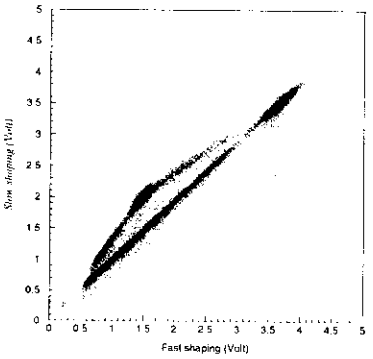

(d) Cs + 1 kHz LED
(Improved circuit)

Figure 15. The deviation of the spectrum of ^{137}Cs in a fast-slow plane, due to injection of 100 MeV deposit signals. The improvement of the front-end electronics can be seen.

desired energy by controlling the pulse height of the signal put onto the LED, and the input rate was controlled by a random pulse generator. We also irradiated a combination of a small GSO and a small BGO crystal attached to the photomultiplier tube by a 662 keV γ-ray from a ^{137}Cs isotope. We kept the ^{137}Cs count rate constant while varying the rate of the 100 MeV pulse, and monitored the change in the spectrum. Since diodes are known to have temperature dependence, we did the measurement in two different temperatures. Onboard the satellite, it is expected to be around $-10°$C .

The spectrum of GSO irraddiated by ^{137}Cs in a fast-slow plane is shown in figure 15. We compared the front-end

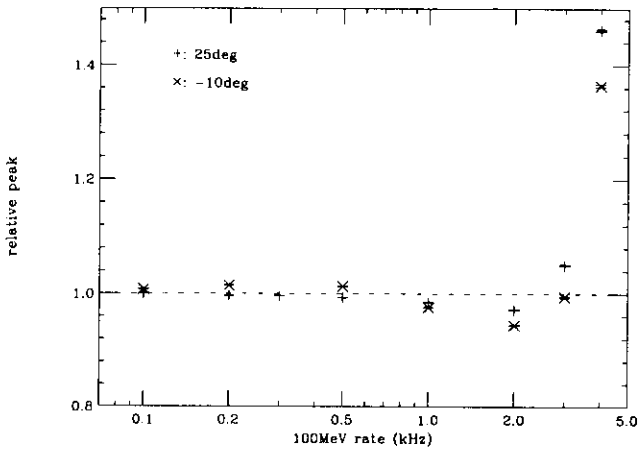

Figure 16. The shift in the peak at high counting rates of a 100 MeV pulse

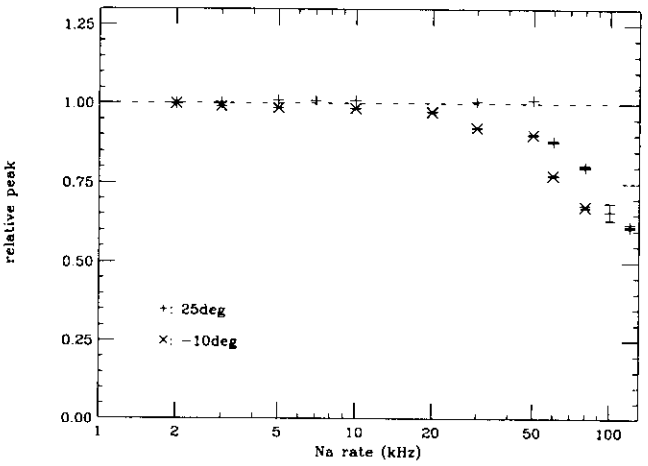

Figure 17. The shift in the peak at high counting rates of a 511 keV pulse

circuit based on the first design and the improved circuit used for the flight model. (a) is the spectrum irradiated only by ^{137}Cs, where the two branches representing BGO and GSO are separated clearly. The branch with the flatter inclination is the GSO events. Panels (b) and (c) shows the spectra with 200 Hz and 1 kHz LED input, using the original circuit. The bottom panels, (d) and (e) shows the spectra using the improved circuit. The improvement in the spectrum is clear. On 1 kHz injection, while the spectrum obtained by using the original circuits shifts and gets out of shape, the spectrum obtained by using the new circuit stays almost at the same position. This is totally due to the quick recovery and the low overshoot pulse height.

The measured peak shift is plotted in figure 16. The horizontal axis is the counting rate of the 100 MeV input signal, and the vertical axis is the relative peak of the ^{137}Cs spectrum. The shift is $\sim$ 1% for 500 Hz input, and 2.5% for 1 kHz input. Since the counting rate of charged particles in orbit are expected to be $\sim$200 Hz at most, this would be sufficient for our purpose. We also found that the peak begins to shift to the higher side at $\sim$4 kHz. This can be understood as follows. When the anode current becomes very large, the bleeder current will be insufficient to generate the proper ladder voltage. Since the total voltage on the bleeder ladder is always constant, the voltage upon the other downstream resistors will be higher, which makes the gain higher. (see figure 24 for the bleeder circuit.)

We also verified the tolerance of our electronics against high counting rates of a normal energy pulses. We used the 511 keV line from a ^{22}Na isotope, and monitored the spectrum as increasing the counting rate by changing the distance of the isotope. The result is shown in figure 17. We can see that the shift in the peak is 1.5 % at 10 kHz, the expected maximum counting rate. Considering that the resolution at this energy is $\sim$10 %, we concluded that this is also a sufficient performance for our observation.

4.1.2. The Vetos in the Flight Model

We must remark that all the results presented so far in this section were obtained without using vetos generated from upper discriminators as in the flight model. The importance is that the change in the spectrum is kept at the above level even without using vetos.

In the flight-model HXD, we have two types of vetos considering large pulses; The upper level discriminator (UD) and the super upper level discriminator (SUD). The former is the regular UD generated from the anode signal, whose threshold is set around 1 MeV. This also prevents triggers due to after pulses of the photomultiplier produced by large signals. The anode amplifier output for a 100 MeV deposit signal is shown in figure 18. The waveform on top is the input of the UD comparator, and the bottom is the output. We can see that many fake pre-trigger signals appear due to after pulses of the photomultiplier, and they are inhibited by the UD veto.

The second one, SUD, is generated from a totally different path. The waveform of the preamplifier output for a 100 MeV deposit pulse is shown in figure 19, together with a 122 keV signal. The comparator is set to detect the overshoot portion of the preamplifier output, and thus the width will be energy dependent. However, since there is a delay of several μsec until the SUD signal is activated, we must guarantee the UD width to be long enough till it is activated.

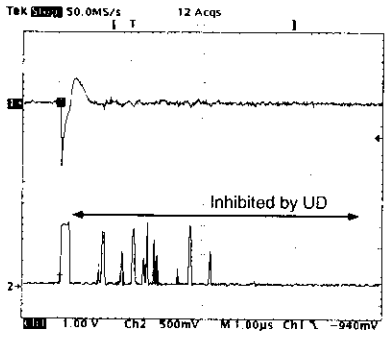

Figure 18. The input (top) and output (bottom) waveforms of the LD comparator for a 100 MeV deposit signal. The number of fake triggers generated by the after pulses of the photomultiplier are inhibited by the UD.

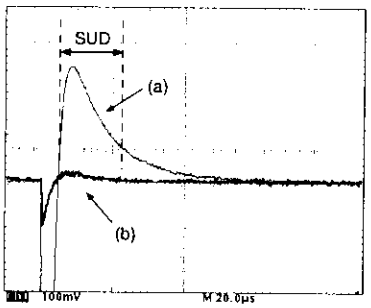

Figure 19. The preamplifier output for a (a) 100 MeV and (b) 122 keV deposit pulse. The signal polarity is negative. We make use of the overshoot (covered with arrows) in order to generate a energy dependent veto signal.

4.1.3. Tests using Charged Particle Beams

Since all the charged particle events in the above discussion were simulated by either LEDs or light pulsers, we also performed two beam tests to see the actual effect. The first one was the proton beam in High Energy Accelerator Research Organization (KEK) in Tsukuba. The main purpose was to verify how long it takes for our electronics to recover after the injection of charged particles, and also reflect it to the width of the vetos in the flight model.

Figure 20 represents the performance against charged particles that we acquired in the second beam test at National Institute of Radiological Science (NIRS). Here, we used the ^{12}C beam with the energy 400 MeV/c. For the electronics, we used the "nearly flight-model" AE module which consists of the same circuit boards as the flight-model AE – the only difference is that not all elements are the MIL standards used in the flight model. For the data acquisition, we used the Ground Support Equipment (GSE) system which was newly developed by our group.[22] The figure shows the spectrum of GSO irradiated by the 662 keV γ-rays from ^{137}Cs . The solid and dotted line respectively represents cases with and without the irradiation by the ^{12}C beam. The shift of the peak is within the error bars, and no particular difference was seen in the spectrum, confirming that the data acquisition system including the vetos is working fine. We also acquired the spectrum without using the vetos, and measured a peak shift of 0.25 %, which is also negligible. The peak height and resolution is summarized in table 4. The counting rate was not very high, ~300 Hz per spill, but considering the counting rate in orbit, this should a reasonable value.

Table 4. The difference of the obtained peak and energy resolution for the 662 keV γ-ray line

Condition	peak (ch)	resolution(FWHM) (%)
Beam off	2418 ± 1	9.6 ± 0.1
Beam on, Veto off	2423 ± 1	9.3 ± 0.1
Beam on, Veto on	2416 ± 1	9.4 ± 0.1

4.2. The PIN Diodes

During passages through the South Atlantic Anomaly, we plan to use the PIN detectors to monitor the counting rate of charged particles. (The high voltages of the photomultiplier tubes will be turned off – the counting rate will be enormous.) Thus, although the volume of the PIN detector is much smaller than the scintillators, we had to guarantee the electronics to maintain its performance against charged particles.

Similar to the bleeders of the phoswich counters, we mounted a clamping stage in the shaping chain to shorten the recovery.[23] In order to see the performance, we generated a 30 MeV deposit pulse by inputing test pulses into the preamplifier, together with the X-ray signal from the PIN detector. We irradiated the PIN detector with an ^{241}Am

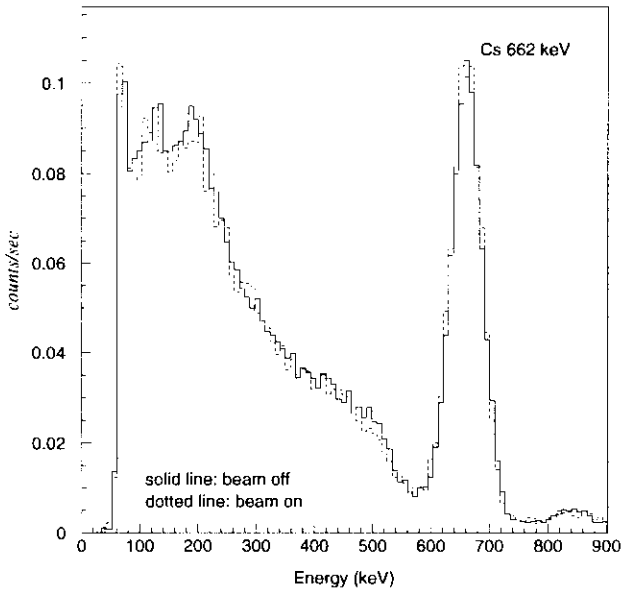

Figure 20. The spectrum obtained by irradiating a 662 keV γ-ray from ^{137}Cs with (dotted line) and without (solid line) the ^{12}C beam. We can see that the spectrum is not affected.

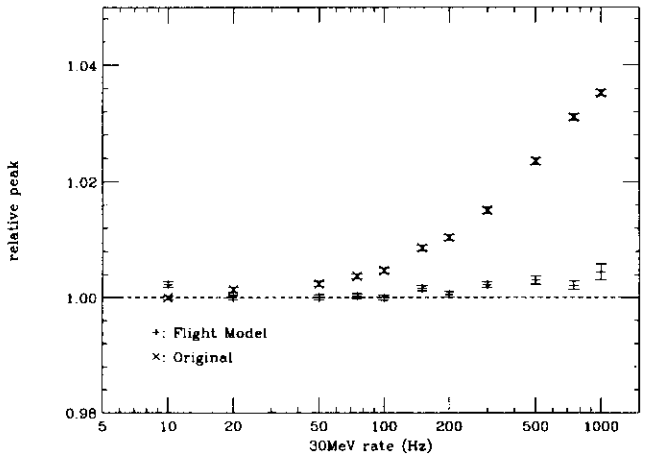

Figure 21. The shift in the peak at high counting rates of a large (30 MeV) pulse

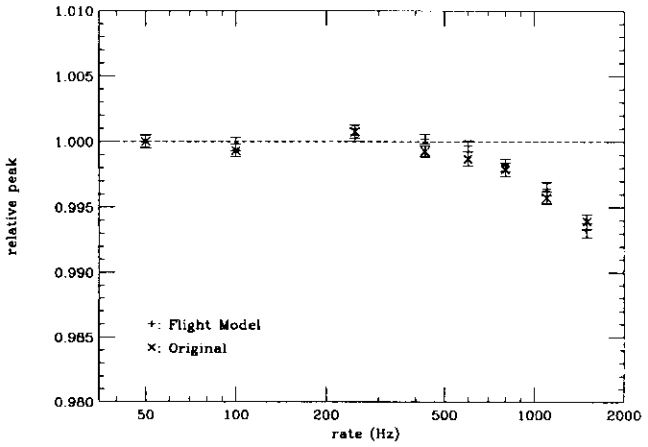

Figure 22. The shift in the peak at high counting rates of a normal (60 keV) pulse

isotope and monitored its spectrum. The result is shown in figure 21. The horizontal axis represents the input rate of the 30 MeV signal, and the vertical axis is the relative peak. We can see that the shift in the peak is much smaller for improved design used in the flight model, which was less than 1% at 1 kHz input.

We also verified the stability against high counting rates of a regular X-ray signal. We monitored the spectrum as increasing the X-ray count rate by closening an ^{241}Am isotope. The result is shown in figure 22. There is not much difference in the two types here, and the shift is the peak is less than 1 % until 2 kHz. Considering the counting rate of the PIN diodes, we regarded the results as a sufficient performance.

5. SUMMARY

The performance of the flight-model HXD was verified, and we confirmed that the background level of both the phoswich counters and PIN doides at sea level is in the lowest level we have reached through out our development.

The expected sensitivity in orbit was calculated based on the results, and the HXD is expected to have the highest sensitivity in the energy range of 10-300 keV. This also confirms that our system is operating properly in selecting only the pure GSO or PIN events. We also obtained the spectrum from line γ-rays and confirmed that the 31 keV line (lowest energy end for the phoswich counters) can be clearly detected.

Considering charged particles, we did careful design on the front-end electronics, and succeeded in reducing the recovery time much shorter than the original design. We verified the stability using the flight-model electronics, and confirmed that our system will maintain its performance within the expected counting rate in space. The tests of the satellite is still underway, preparing for the launch in January, 2000.

APPENDIX A. THE BLEEDER DESIGN

The bleeder is the very front electronics where the high voltage is divided by ladders of resistors to be put onto each electrodes in the photomultiplier tubes. The voltage division ratio is followed by the HAMAMATSU catalog (R6231-07), and the resistance values are set high, 1 MΩ, so as to reduce power.

As described in figure 23(a), a capacitor is mounted at the output of the bleeder to decouple the high voltage (C_c). This may be needless if the photomultiplier tube is operated in negative high voltage, but this is not preferred because the high voltage will be put very near the photo cathode, and atmospheric discharge may occur.

Since the charge at the dynode or anode is divided to the capacitor (C_c) and the resistance (R_a) by their impedance ratio, a large capacitor is preferred to extract all the charge. On the other hand, the discharging time is given by the product of this capacitor (C_c) and the feedback resistance of the preamplifier (R_f). Thus we lowered the values of the capacitors and resistors as small as possible, but not affecting the performance to normal γ-rays. We found that we can reduce the recovery time to 130 μs by lowering the decoupling capacitors and and resistors, which is shown in figure 23(b). However, we can also see that the overshoot has become larger.

We found that this overshoot results mainly from the the capacitance and zener diode mounted in the bleeder ladder, which shifts the voltage on B together with A. When a large current flows, the charge at the anode discharges rather quickly, but since the charge at the dynode C_c must discharge via the bleeder ladder, it causes a long positive signal. We also verified that the overshoot will be prevented if we take away the capacitor and zener diode away. However, the zener cannot be taken away in order to keep gain stability. Thus we planned to install a clamping stage at the output so as to discharge quick at large inputs, as written below.

In order to discharge only in case of large signals, we first tried mounting a zener diode parallel to the resistors (R_a in figure 23(a)) In this case, the clamping begins to work when the current increases and the voltage on R_a reaches the zener voltage. The effect of the clamp was evident, with smaller and shorter overshoot. However, although this behaved very well for large pulses, there was a problem that the capacitance of the zeners are large (~100 pF) that the charge would be separated to the zener and the output. This reduces the pulse height of the extracted signal, which is undesirable. We tried preventing this by several ways, adding extra parts, but they all had merits and demerits.

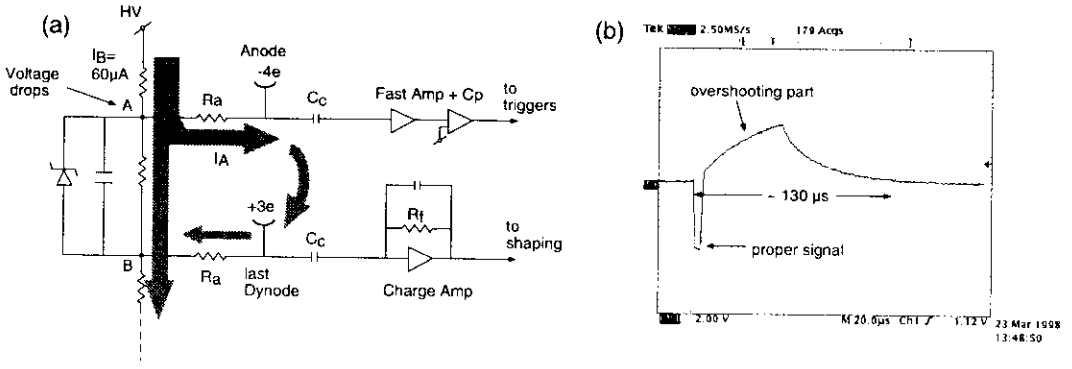

Figure 23. The current flow of the last two stages of the bleeder (a) and the waveform of the preamplifier output for a 100 MeV pulse using the bleeder revised by adjusting the values of capacitors and resistors. (b)

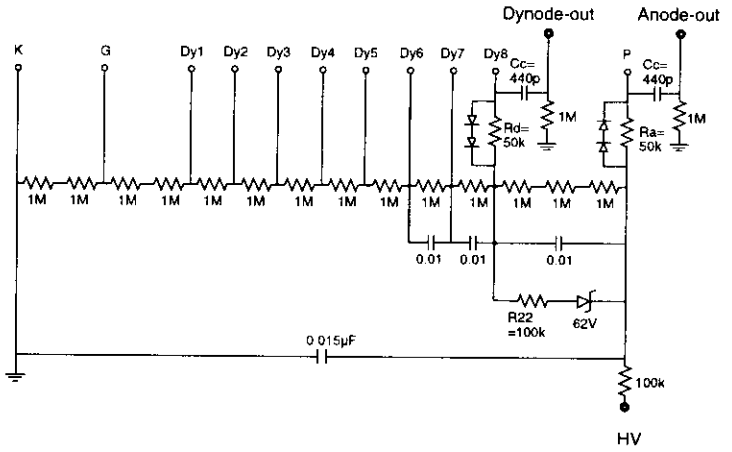

Figure 24. The circuit diagram of the improved bleeder used the flight-model HXD.

Thus we concluded to use a regular diode - the capacity is as small as ~2 pF. The concern was the voltage 0.7 V too low for the beginning of the diode clamp, so we put two diodes in serial. We also lowered R_a from 100 kΩ to 50 kΩ. This will retard the begging of the clamp for DC currents. (It is the same for AC currents because the impedance lowers, and twice current flows to the R_a.) We found that the recovery is even quicker than the case using a zener. The output waveform for a 100 MeV deposit pulse is shown in figure 14. We can see that the overshoot pulse height which used to be 3.5 V is reduced to ~250 mV, less than one order of magnitude, and the recovery time from 130 μs to 50 μs.

A.1. The Limit of the Anode Current

Since the current must conserve in the bleeder, (figure 23(a)), we can consider the anode current (and the in-pipe current) a portion of the bleeder current flowing in a different path, and thus it should have a limit depending on the bleeder current.

In order to see where the limit of the anode current is, we used a Light Emitting Diode (LED) to inject a constant light into the photomultiplier tube. This will produce a DC anode current, which is easier to monitor. We also irradiated a combination of a small GSO and small BGO attached to the photomultiplier tube, by a 662 keV γ-ray from ^{137}Cs. We kept the γ-ray counting rate constant, and monitored the γ-ray spectrum while increasing the intensity of the LED. We also monitored the voltage upon R_a so as to measure the anode current at each moment.

The resulting plot for the original and new bleeder is shown in figure 25. The horizontal axis is the calculated anode current from the measured voltage upon R_a and the vertical axis is the relative peak of 662 keV in the acquired ^{137}Cs spectrum. We found that the pulse height begins to decrease when the anode current reaches ~ 15 μA, using

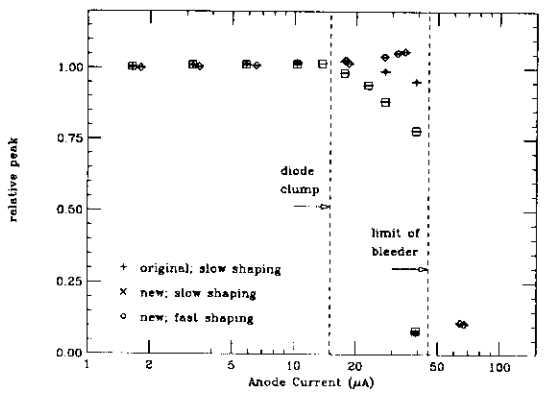

Figure 25. The limit of the anode current in the bleeder using the diode clamped bleeder.

the diode-clamp bleeder. This is expected to be where the diode clamp begins to work. We also found that the effect is smaller for the faster shaping pulse. This can be understood considering that the diode clamp is equivalent to a differentiation stage, which starts to work when a large signal injects. This also indicates that in case the anode current happens to increase by very high counting rates in space, we can at least use the fast shaping for pulse height information.

ACKNOWLEDGMENTS

This research was partially supported by Fellowships of the Japan Society for Promotion of Science for Japanese Young Scientists, Grant-in-Aid for Scientific Research No. 05242101, and also Grant-in-Aid for COE Research No. 07CE2002 by the Ministry of Education, Culture and Science, Japan.

REFERENCES

1. Inoue, H., "The Astro-E Mission", *Proc. of the 11th Colloquium on UV and X-Ray Spectroscopy of Astrophysical and Laboratory Plasmas*, Universal Academy Press, pp. 239-241 (Tokyo, 1995)
2. Ogawara, Y., "Astro-E Mission", *Proc. of IAU Symposium no. 188*. (Kyoto, 1998)
3. Takahashi, T., Inoue, H., and Ogawara, Y., "Astro-E Mission and the X-ray Survey", *Astron. Nachr.*, **319**, 3, pp. 159-162 (1998)
4. Kamae, T., et al., "Well-type Phoswich Counters for Low-Flux X-Ray/γ-Ray Detection", *SPIE*, **1734**, pp. 2-13 (1992)
5. Takahashi, T., et al., "New Hard X-ray/Gamma-ray Detector — Welcome-1 —", *SPIE*, **1734**, pp. 44-55 (1992)
6. Kamae, T., et al., "Well-type Phoswich Counters for Low-Flux X-Ray/γ-Ray Detection", *IEEE Trans. Nucl. Sci.*, **40**, 204(1993)
7. Takahashi, T., et al., "Newly Developed Low Background Hard X-ray/Gamma-ray Telescope with the Well-tye Phoswich Counters", *IEEE Trans. Nucl. Sci.*, **40**, 890-898 (1993)
8. Hayashida, K., et al., *Publ. Astr. Soc. Japan*, **41** 373 (1989)
9. Tsukada, K., Ikeda, H., Kamae, T., Takahashi, T., and Murakami, H., "Peak Hold Monolithic Integrated Circuit with Build-in Shaping Amplifier for Hard X-ray Detector", *IEEE Trans. Nucl. Sci.*, **NS-40**, 724 (1993)
10. Kaneda, H., et al., "Development of the hard x-ray detector for the ASTRO-E mission", *SPIE*, **2518**, pp. 85-95 (1995)
11. Takahashi, T. et al., "Development of the hard X-ray detector for the ASTRO-E mission", *Astron. Astrophys. Suppl.*, **120**, pp.645-648 (1996).
12. Tsuchida, N., Ikeda, M., Kamae, T., and Kokubun, M., "Temperature Dependence of Gamma Ray Excited Scintillation Time Profile and Light Yield of GSO, YAP AND BGO", *Nucl. Instr.Meth.*, **A385**, 290-298 (1996)
13. Ezawa, H., et al., "Development of the Pulse-Shape Discrimination LSI for ASTRO-E Hard X-ray Detector", *IEEE Trans. Nucl. Sci.*, **NS-43**, pp. 1521-1526 (1996)
14. Ozawa, H., et al., "Integration of the readout electronics for the Astro-E Hard X-ray Detector", *SPIE*, **3115**, pp. 235-243 (1997)
15. Sugizaki, M. et al., "Development of the large area silicon PIN diode with 2mm-thick depletion layer for Hard X-ray Detector (HXD) on-board Astro-E", *SPIE*, **3115**, pp. 244-253 (1997).
16. Kokubun, M., et al., *IEEE Trans. Nucl. Sci.*, 1999. (in press)
17. Johnson, W. N., et al., "The Oriented Scintillation Spectrometer Experiment Instrument Description", *Astrophys. J. Suppl.* 86, 693-712 (1993)
18. HEXTE instrumental team "The XTE Technical Appendix" http://mamacass.ucds.edu/
19. Rothschild, R.,E., et al, *Astrophys. J.*, 496, 538-549, 1998
20. Institute of Space and Astronautical Science, Astro-E Interim Report SES-TD-98-004 (1998)
21. Takahashi, T., et al., "The Electronic System for the Astro-E Hard X-Ray Detector", *SPIE*, **3445** (1998)
22. Kataoka, J., et al., "Verification of the Astro-E hard x-ray detector based on a newly developed ground support electronics", *SPIE*, 3445 (1998)
23. Tanihata, C., Master Thesis, University of Tokyo, 1999
24. Nakazawa, N., et al., "Fabrication of the Astro-E Hard X-Ray Detector" in this volume